University of Groningen

HST imaging of four gravitationally lensed quasars

Bate, N. F.; Vernardos, G.; O'Dowd, M. J.; Neri-Larios, D. M.; Webster, R. L.; Floyd, D. J. E.; Barone-Nugent, R. L.; Labrie, K.; King, A. L.; Yong, S. -Y.

IMPORTANT NOTE: You are advised to consult the publisher's version (publisher's PDF) if you wish to cite from it. Please check the document version below.

Document Version
Publisher's PDF, also known as Version of record

Link to publication in University of Groningen/UMCG research database

HST imaging of four gravitationally lensed quasars

N. F. Bate,[1]★ G. Vernardos,[2] M. J. O'Dowd,[3,4,5] D. M. Neri-Larios,[6] R. L. Webster,[6] D. J. E. Floyd,[6,7,8,9] R. L. Barone-Nugent,[6] K. Labrie,[10] A. L. King[6] and S.-Y. Yong[6]

[1]*Institute of Astronomy, University of Cambridge, Madingley Road, Cambridge CB3 0HA, UK*
[2]*Kapteyn Astronomical Institute, University of Groningen, PO Box 800, NL-9700AV Groningen, the Netherlands*
[3]*Department of Physics and Astronomy, Lehman College, City University of New York, 250 Bedford Park Boulevard West, Bronx, NY 10468-1589, USA*
[4]*Department of Astrophysics, American Museum of Natural History, Central Park West and 79th Street, NY 10024-5192, USA*
[5]*The Graduate Center of the City University of New York, 365 Fifth Avenue, New York, NY 10016, USA*
[6]*School of Physics, The University of Melbourne, Parkville, VIC 3010, Australia*
[7]*School of Physics, Monash University, Clayton, VIC 3800, Australia*
[8]*Monash Centre for Astrophysics, Monash University, Clayton, VIC 3800, Australia*
[9]*Think Big Analytics, 3 London Bridge Street, London SE1 9SG, UK*
[10]*Gemini Observatory, Hilo, HI 96720, USA*

ABSTRACT

We present new *Hubble Space Telescope* WFC3 imaging of four gravitationally lensed quasars: MG 0414+0534; RXJ 0911+0551; B 1422+231; WFI J2026-4536. In three of these systems we detect wavelength-dependent microlensing, which we use to place constraints on the sizes and temperature profiles of the accretion discs in each quasar. Accretion disc radius is assumed to vary with wavelength according to the power-law relationship $r \propto \lambda^p$, equivalent to a radial temperature profile of $T \propto r^{-1/p}$. The goal of this work is to search for deviations from standard thin disc theory, which predicts that radius goes as wavelength to the power $p = 4/3$. We find a wide range of power-law indices, from $p = 1.4^{+0.5}_{-0.4}$ in B 1422+231 to $p = 2.3^{+0.5}_{-0.4}$ in WFI J2026-4536. The measured value of p appears to correlate with the strength of the wavelength-dependent microlensing. We explore this issue with mock simulations using a fixed accretion disc with $p = 1.5$, and find that cases where wavelength-dependent microlensing is small tend to underestimate the value of p. This casts doubt on previous ensemble single-epoch measurements which have favoured low values using samples of lensed quasars that display only moderate chromatic effects. Using only our systems with strong chromatic microlensing we prefer $p > 4/3$, corresponding to shallower temperature profiles than expected from standard thin disc theory.

Key words: accretion, accretion discs – gravitational lensing: micro – quasars: individual: MG 0414+0534 – quasars: individual: RXJ 0911+0551 – quasars: individual: B 1422+231 – quasars: individual: WFI J2026-4536.

1 INTRODUCTION

Observations of gravitationally microlensed quasars offer a unique opportunity to study the structure of quasar accretion discs at rest frame ultraviolet (UV) and optical wavelengths. These analyses hinge on the fact that gravitational lensing is achromatic, but the magnitude of any microlensing-induced brightness fluctuations depends strongly on the projected size of the emission region in the lensed source. In a quasar accretion disc, hotter regions are expected to be physically smaller than cooler regions, and so will be more strongly magnified by microlensing.

Microlensing analyses have already thrown up challenges to the standard thin disc theory. It has been robustly established that quasar accretion discs in the observed optical (2500 Å rest frame) are larger by factors of 2 to 4 than expected. This result is obtained from both single-epoch observations, and light-curve analyses. In the latter case (e.g. Morgan et al. 2010; the review of Chartas et al. 2016 and references therein), observationally expensive monitoring campaigns are conducted to gather microlensing light curves, typically focused on accretion disc sizes at single, or occasionally two, wavelengths (usually X-ray and optical). Single-epoch studies (e.g. Pooley et al. 2007; Blackburne et al. 2011; Jiménez-Vicente et al. 2012) allow for easier analysis of larger samples of objects, and return similar results.

★ E-mail: nfbate@gmail.com

When multiwavelength data are available, quasar microlensing observations can be used to map the radial profile of the accretion disc as a function of wavelength (Anguita et al. 2008; Bate et al. 2008; Eigenbrod et al. 2008; Floyd, Bate & Webster 2009; Blackburne et al. 2011; Blackburne et al. 2014; Jiménez-Vicente et al. 2014; Rojas et al. 2014; MacLeod et al. 2015). Typically, a power-law of the form $r \propto \lambda^p$ is assumed. The standard Shakura & Sunyaev (1973) disc sets $p = 4/3$ (hereafter SS), but other models predict different values for p (e.g. Abramowicz et al. 1988, $p = 2.0$; Agol & Krolik 2000, $p = 8/7$).

Under the assumption that the emergent accretion disc spectrum is the superposition of blackbody spectra generated locally in the disc, the spectral profile $r \propto \lambda^p$ is related to the temperature profile via the power-law index p: $T \propto r^{-1/p}$ (see e.g. Frank, King & Raine 2002). Constraints on the power-law index of the spectral profile are therefore also constraints on the radial temperature profile. If $p > 4/3$, temperature falls off as a function of radius more slowly than expected from the SS disc (a shallower temperature profile). If $p < 4/3$, the temperature profile is steeper and cools down more rapidly with radius than the SS disc .

Early temperature profile measurements using microlensing have painted a conflicting picture. Single-epoch observations of microlensed accretion discs seem to favour steeper temperature profiles than SS ($p < 4/3$, e.g. Floyd et al. 2009; Blackburne et al. 2011; Muñoz et al. 2011; Jiménez-Vicente et al. 2014), although there are exceptions (e.g. Bate et al. 2008; Rojas et al. 2014). This is difficult to reconcile with measurements of larger than expected discs at optical wavelengths, since a steeper temperature profile implies that the accretion disc will be smaller at a given wavelength, not larger.

Most temperature profile measurements have been performed on single systems, or occasionally a handful. The most recent ensemble measurement is Jiménez-Vicente et al. (2014), hereafter JV14, who analysed 10 image pairs in eight lensed quasars. They found a joint Bayesian estimate for the power-law index of $p = 0.8 \pm 0.2$ at 68 per cent confidence, well below the fiducial $p = 4/3$.

Gravitational microlensing is currently the only technique that has been used to study the physical structure of these objects at high redshifts ($z \sim 1.5$–3.5). Photometric reverberation mapping has been used to probe accretion discs in lower-redshift active galactic nuclei (AGNs). The AGN Space Telescope and Optical Reverberation Mapping project has examined the accretion disc in the Seyfert NGC 5548 in considerable detail (see especially Fausnaugh et al. 2016; Starkey et al. 2017), using 19 overlapping continuum light curves to measure a larger size and steeper temperature profile ($p = 1.01 \pm 0.03$) in that system. A similarly detailed analysis of NGC 4593 (Cackett et al. 2017) also found a larger than expected size, but the measured temperature profile was consistent with the standard thin disc prescription. Jiang et al. (2017) analysed a sample of 240 $z \sim 0.1$–0.3 quasars from Pan-STARRS. They again measure larger accretion disc sizes than expected from thin-disc theory, however they favour flatter temperature profiles (with the caveat that their wavelength coverage is much shorter than the Starkey et al. 2017 or Cackett et al. 2017 analyses).

Understanding the diversity of temperature profile measurements, along with the apparent contradiction between larger discs and (possibly) steeper temperature profiles requires more data, and careful consideration of sources of error and contamination in both our observations and our analysis techniques. The principle contaminants in single-epoch observations are: time delays between lensed images causing us to catch the background quasar in different underlying states; broad emission lines that fall in broad-band filters

and dilute the signal from the quasar continuum; and differential extinction. Possible systematic effects have been poorly explored.

In this paper, we present multiwavelength *Hubble Space Telescope* (*HST*) observations of four gravitationally lensed quasars: MG 0414+0534 (Hewitt et al. 1992), RXJ 0911+0551 (Bade et al. 1997), B 1422+231 (Patnaik et al. 1992), and WFI J2026-4536 (Morgan et al. 2004). These observations were tuned to mitigate some of the major challenges and sources of uncertainty facing multiband single-epoch imaging analyses.

In Section 2, we discuss issues around our sample selection, including common contaminants in single-epoch microlensing analyses. We also present background detail on the four lensed quasars studied here, summarizing any existing microlensing analyses. In Section 3, we present our data, and describe the reduction process. In Section 4, we lay out our simulation technique. First, we discuss macrolens models for each of our systems, then the single-epoch microlensing analysis technique. This technique broadly follows JV14 but differs in a few key details. In Section 5, we present the results of our analysis, and then discuss their implications in Section 6. This discussion leads to a suite of mock observations in Section 7, which clarify the origin of the steep temperature profiles measured in JV14. Finally, we conclude in Section 8.

Throughout this paper, we use a cosmology with $H_0 = 72 \, \mathrm{km \, s^{-1} \, Mpc^{-1}}$, $\Omega_\mathrm{m} = 0.3$, and $\Omega_\Lambda = 0.7$.

2 SAMPLE SELECTION

In this section, we discuss common issues relating to the single-epoch imaging technique, including methods for their mitigation. We then present our *HST* sample of four gravitationally lensed quasars, and briefly discuss any previous microlensing analyses of these systems.

2.1 Single-epoch imaging technique contaminants

Single-epoch imaging studies of quasar microlensing are subject to a number of potential contaminants, which have been successfully handled to a greater or lesser degree. The principle contaminants in the observations are: (i) time delays between lensed images; (ii) broad emission lines that fall in broad-band filters and dilute the signal from the quasar continuum; and (iii) differential extinction. Finally, (iv) possible systematic effects in our analysis technique have been poorly explored. We will discuss each of these issues in turn, focussing on how we have mitigated them in the current analysis.

(i) Quasars are variable on all time-scales longer than a day (MacLeod et al. 2012), and so time delays between lensed images can mean that the background quasar is captured in a different state in each image with a single observation. In order to eliminate quasar variability as a source of contamination, we work only with close image pairs. In these cases, time delays are expected to be short (less than a day), and so we can be confident that the quasar is in the same state in each image.

Close image pairs provide an ideal laboratory for microlensing constraints on quasar accretion discs (Bate, Webster & Wyithe 2007; Bate et al. 2008; Floyd et al. 2009). In the presence of a high smooth matter fraction – expected in the outskirts of lensing galaxies, where lensed quasar images typically form – one of the close images (the saddle point image) is preferentially suppressed by microlensing (Schechter & Wambsganss 2002; Vernardos et al. 2014). This frequently leads to a large magnification difference between

the close images, which produce the tightest single-epoch accretion disc size constraints. It is often overlooked that, conversely, small magnification differences between lensed images provide very little information on accretion disc sizes (see fig. 4 in Bate et al. 2007). With their <0.5 arcsec separation, deblending of close image pairs is a significant challenge with ground-based imaging. For this reason, the photometric precision afforded by *HST* is essential.

(ii) Measurements of the continuum slope with broad multiband photometry risk line contamination, which arises due to differing physical scales for broad line and continuum emission in the source quasar. Since broad lines are expected to be emitted from larger physical scales than the continuum, they will be affected by microlensing differently (see e.g. Abajas et al. 2002; Wayth, O'Dowd & Webster 2005; O'Dowd et al. 2011; Sluse et al. 2012b). If a broad-band filter overlaps a broad emission line, the flux you observe in that filter is therefore a combination of broad line and continuum emission, and so convolves microlensing information on two physical scales.

Line contamination can be avoided with sufficient spectral resolution. However, this does not necessitate full spectroscopy. Narrow- or medium-band filters can be chosen to cleanly select regions of the quasar spectrum free from broad line contamination (e.g. Mosquera et al. 2011). This approach grants higher signal to noise for a given exposure time than spectroscopy, and also greatly simplifies the deblending of close lensed image pairs. This is the approach we have chosen, using medium-band *HST* filters to minimize the impact of broad emission lines on our results.

(iii) Differential extinction can produce chromatic variation that mimics the effects of microlensing (see e.g. O'Dowd et al. 2018). This can be effectively removed by monitoring the system and conducting light-curve analyses: differential extinction is not expected to vary on microlensing-like time-scales.

Accounting for it in single-epoch observations is much harder. In the ideal case, we would have observations of regions in the quasar that are sufficiently large to be unaffected by microlensing, emitting at wavelengths very similar to the continuum, to establish the baseline impact of differential extinction. For example, Mediavilla et al. (2009) and JV14 use the narrow component of broad emission lines to estimate intrinsic flux ratios. In the absence of adequate spectroscopy, infrared or radio flux ratios can be used to estimate intrinsic magnification ratios. This is the method we adopt here.

(iv) The final issue is systematics in our simulation technique, and it remains relatively unexplored. Single-epoch analyses have proceeded under the assumption that the simulations provide a clean measurement of the structure of the quasar accretion disc, if contaminants in the observational data are minimized. In this paper, we will present the first evidence that this assumption may not be strictly true.

This last issue will be particularly important in the forthcoming synoptic survey era. Currently, we have temperature profile measurements for only a handful of lensed quasars; only ∼100 are known (see Mosquera & Kochanek 2011 for a compilation). The Large Synoptic Survey Telescope (LSST; LSST Science Collaboration et al. 2009) alone is expected to discover thousands more (Oguri & Marshall 2010), enabling studies of true statistical samples. Future surveys may provide us with light curves of these systems, superseding the single-epoch technique. However, the time-scales for microlensing variations are often years or decades, and so there will still be a use for single-epoch analyses for the foreseeable future.

2.2 *HST* sample

The four lensed systems studied here were specifically chosen from a larger programme to have no obvious ring features in our data. The presence of full or partial Einstein rings indicates that the quasar host galaxy is being significantly lensed. Rings or arcs provide more constraints for modelling the lens, however they may be an additional source of contamination in any measured flux ratios between lensed images. This issue will be explored in more detail in subsequent papers.

2.2.1 *MG 0414+0534*

This system, first reported in Hewitt et al. (1992), has been the subject of a significant number of lensing analyses. This is in part due to an anomaly in the flux ratio between images A_2 and A_1 that persists into the infrared and the radio. This has been taken to indicate the presence of unobserved substructure in the lens, on so-called millilensing scales (approximately dwarf galaxy-sized, see e.g. Mao & Schneider 1998; Dalal & Kochanek 2002; Kochanek & Dalal 2004; MacLeod et al. 2013).

In Pooley et al. (2007), the authors used X-ray and optical data to study the relative sizes of the accretion discs in 10 systems, including MG 0414+0534. They found that the optical continuum emission in this quasar arose from a region ∼3 times larger than expected from thin disc theory. Blackburne et al. (2011) followed up this analysis by also constraining the temperature profile of the accretion disc, finding a value consistent with the SS $p = 4/3$ scaling. It is worth noting that this result was at odds with all of the other systems in their paper, for which they found very low values of $p \sim 0.2$. An X-ray microlensing size measurement of MG 0414+0534 also appears in Jiménez-Vicente et al. (2015b).

We have also previously studied the accretion disc in MG 0414+0534 (Bate et al. 2008; Bate et al. 2011). Although the errors in our previous analysis were large, we found an accretion disc temperature profile formally consistent with the SS disc at the 2σ level, with a preference for power-law indices $p > 4/3$ (formal constraint: $1.6^{+0.6}_{-0.5}$ at 68 per cent confidence). Our analysis was conducted with an earlier version of the single-epoch imaging technique, which did not account for errors in macromodelling. Given the possible presence of substructure near the A_2/A_1 image pair, this omission may be significant.

2.2.2 *RXJ 0911+0551*

RXJ 0911+0551 is an X-ray bright lensed quasar originally detected in the *ROSAT* All-Sky Survey (Bade et al. 1997). It has appeared in the X-ray accretion disc analyses of Pooley et al. (2007), Blackburne et al. (2011), and Jiménez-Vicente et al. (2015b). In Pooley et al. (2007), the quasar was found to have an optical accretion disc size ∼6 times larger than expected from thin disc theory.

Using optical, IR, and X-ray data, Blackburne et al. (2011) reported a temperature profile for this system consistent with no wavelength dependence ($p = 0.17 \pm 0.41$). These particularly low values of p (corresponding to steep temperature profiles) were the overall result for their analysis of 12 systems.

2.2.3 *B 1422+231*

B 1422+231 (Patnaik et al. 1992) is also part of the Pooley et al. (2007) sample of lensed quasars. It differs from MG 0414+0534 in that its optical size measurement is apparently consistent with thin
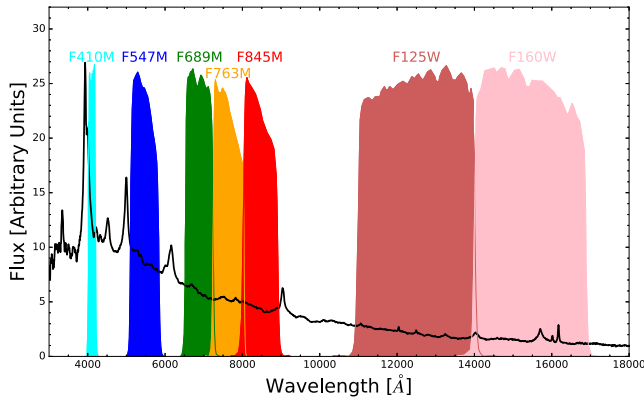
Figure 1. *HST* WFC3 filter transmission curves, overlaid on a quasar composite spectrum (Vanden Berk et al. 2001) at the redshift of WFI J2026-4536($z = 2.23$). This illustrates how we have used medium-band filters to select regions between broad emission lines, to avoid contaminating the signal from the microlensed accretion disc.

disc theory. It is also included in the joint size analyses of Mediavilla et al. (2009), Jiménez-Vicente et al. (2012), Jiménez-Vicente et al. (2015a), and Jiménez-Vicente et al. (2015b) (the first three using optical data, the latter X-ray), but to date no temperature profile measurement has been reported.

Mao & Schneider (1998) used anomalies in the radio flux ratios to argue for the presence of substructure in the lens. This was the first time that this use for lensed quasar observations was explicitly discussed in the literature. Our lens models are discussed in Section 4.1; for this system, we make no attempt to account for millilensing substructure.

2.2.4 WFI J2026-4536

WFI J2026-4536 is the most recently discovered system in this paper (Morgan et al. 2004), and has only appeared in one microlensing accretion disc analysis: Blackburne et al. (2011). They again found an extremely steep temperature profile, consistent with no wavelength dependence ($p = 0.27 \pm 0.53$).

Additionally, Sluse et al. (2012a) reported that WFI J2026-4536is a problematic system to model. This will be discussed further in Section 4.1. The system's lens redshift is currently unknown.

3 DATA

Observations were taken in *HST* Cycle 20 (Program ID 12874, PI Floyd). Imaging was performed with *HST*'s Wide Field Camera 3 (WFC3) in both the UVIS and IR channels, utilizing four to seven medium-band filters for each target. Medium-band imaging allows us to select filters that fall between broad emission lines. This is important because the broad emission line region is much larger than the accretion disc and so experiences different microlensing magnification (when it is microlensed at all). The suite of WFC3 medium band filters allows us to avoid these lines at all source redshifts. Fig. 1 shows the example case of WFI J2026-4536: filter transmission curves are overlaid on a composite quasar spectrum (Vanden Berk et al. 2001) at this quasar's redshift. Table 1 details exposure times, dates, and filters for each source.

Data were reduced using the standard *HST* Astrodrizzle reduction pipeline. Fluxes of individual lensed images were measured using GALFIT (Peng et al. 2002) to fit a point spread function (PSF) at

the location of each lensed image, while the lensing galaxy was fit with a Sersic profile. Free parameters in the fit included lensed image and lensing galaxy fluxes as well as positions of all sources. TinyTim (Krist, Hook & Stoehr 2011) was used to generate WFC3 PSFs, and StarFit (Timothy Hamilton, private communication) was used to propagate these PSFs through the dither-combine pipeline to match the final combined PSFs. Table 2 gives the measured magnitudes for all lensed images and lensing galaxies.

In Table 3, we present observed magnitude differences for the image pairs of interest (typically the close image pair). The observed wavelengths are taken to be the pivot wavelengths of each filter. These are the data that are used for the microlensing analysis presented in this paper.

4 MODELLING AND SIMULATIONS

In this section, we describe the various components of our lens modelling and microlensing simulation technique.

4.1 Lens models

Models of the lensing potentials in each system provide us with the key parameters for microlensing simulations: the convergence κ and shear γ at each lensed image position.

4.1.1 MG 0414+0534

MG 0414+0534 is known to harbour substructure in the vicinity of the anomalous A_1 and A_2 image pair. Simple lens models consisting only of a singular isothermal ellipse and external shear do not reproduce the A_2/A_1 flux ratios observed in the radio and mid-IR (e.g Katz, Moore & Hewitt 1997; Minezaki et al. 2009). MacLeod et al. (2013) used these data to search for the best-fitting location for a dark substructure near the anomalous image pair. They found a best-fitting mass of $10^{6.2}M_\odot$ to $10^{7.5}M_\odot$, located to the north-east of image A_2 (modelled as a singular isothermal sphere at the redshift of the lensing galaxy).

We take the MacLeod et al. (2013) G1+G2+G3 model using both mid-IR and radio data (see their Table 4, repeated here in Table 5), and calculate convergences and shears at the A_1 and A_2 image positions using LENSMODEL[1] (Keeton 2001). This model includes three lenses: the primary lens galaxy G1, a secondary nearby (observed) galaxy G2, and the (dark) substructure G3 discussed in the previous paragraph. The microlensing parameters for this model are provided in Table 4.

4.1.2 RXJ 0911+0551and B 1422+231

For RXJ 0911+0551 and B 1422+231, we use lens models from the literature (Schechter et al. 2014). These models consist of a singular isothermal ellipsoid (SIE) with an orientation and ellipticity constrained to match the observed shape of the stellar component in each lensing galaxy, plus an external shear term (referred to as SIE+X or SIE+γ models). The RXJ 0911+0551model also includes a secondary lens at the position of an observed smudge in the system, modelled as a singular isothermal sphere (Blackburne et al. 2011). The model parameters are reproduced in Table 5 for convenience, and their resulting convergences and shears are summarized in Table 4.

[1] http://physics.rutgers.edu/~keeton/gravlens/2012WS/

Table 1. *HST* WFC3 observation details.

System	z_S	z_L	Obs. date	Orbits	WFC3/UVIS	WFC3/IR
MG 0414+0534	2.64	0.96	2013-07-25	2	F763M F845M	F125W F160W
RXJ 0911+0551	2.80	0.77	2012-10-19	2	F547M F621M F689M F845M	F125W F160W
B 1422+231	3.62	0.34	2013-07-12	2	F621M F763M F845M	F105W F125W F160W
WFI J2026-4536	2.23	–	2012-11-22	2	F410M F547M F689M F763M F845M	F125W F160W

4.1.3 WFI J2026-4536

WFI J2026-4536 is a slightly more complicated case. Both Chantry, Sluse & Magain (2010) and Sluse et al. (2012a) found this system difficult to fit accurately with simple lens models. In Chantry et al. (2010), they chose to constrain the ellipticity and position angle of an SIE+X lens model by the light (similar to the models in Schechter et al. 2014). Imposing these constraints resulted in a large formal χ^2; models with a significant offset between the position angles of the mass and the light were preferred. In Sluse et al. (2012a), they relaxed these constraints and also added a second mass component to describe a nearby galaxy. In this case they again preferred models where the mass and light are significantly misaligned, possibly hinting at the presence of dark substructures.

In light of these complications, we opted to generate a simple SIE+X model where we left the orientation and the ellipticity of the lens as free parameters. We kept the position of the lens fixed to the centre of the light profile, and used only the image positions as constraints. The best-fitting model, generated with the LENSMODEL code, is provided in Table 5. It is similar to the SIE+X case in Sluse et al. (2012a). We emphasize that this model should be considered illustrative; it does not include the full complexities of the system.

The WFI J2026-4536 lens redshift is also currently unknown. To convert our measured sizes into physical parameters we adopt a lens redshift of $z_{l,\,2026} = 1.04$, estimated from the image separations and probability distributions for z_l (Ofek, Rix & Maoz 2003; Mosquera & Kochanek 2011).

4.2 Simulation technique

We broadly follow the simulation technique laid out in JV14, with two important differences. The technique is described below, highlighting the areas where our methods differ. The basic outlines are

(i) Generate magnification maps from lens models.

(ii) Isolate the microlensing signal from macrolensing using infrared or radio observations.

(iii) Conduct Bayesian microlensing simulations to extract accretion disc parameters.

4.2.1 Magnification maps

The lens models described in the previous section provide the two key microlensing parameters at the location of each lensed image: the convergence κ and shear γ (see Table 4). The convergence can be split into two components: a clumpy component κ_* that describes point-mass (stellar) microlenses, and a smooth component κ_s, such that $\kappa = \kappa_* + \kappa_s$. The smooth matter fraction is $s = \kappa_s/\kappa$.

In the systems studied here, the lensed images lie in the outskirts of the lens galaxies, so we expect the smooth matter fraction to be high. Typical values obtained from previous microlensing analyses range from smooth matter fractions of ∼80 per cent (e.g Bate et al. 2011; Jiménez-Vicente et al. 2015a) to ∼93 per cent (e.g. Pooley et al. 2012). JV14 took the smooth matter fraction to be 95 per cent

in their analysis; we chose instead to vary it. We used 11 smooth matter fractions $s = 0.0, 0.1, 0.2, \ldots, 0.9, 0.99$, and discuss the impact of smooth matter fraction on our results below. This is the first key difference between our analysis and that of JV14.

Magnification maps were generated using the GPU-D code (Thompson et al. 2010; Bate & Fluke 2012), within the GER-LUMPH framework (Vernardos et al. 2014; Vernardos et al. 2015). We used maps with a side length of 100 Einstein radii, and 10 000 pixels, and $M_{micro} = 1M_\odot$ microlenses. This corresponds to physical per-pixel resolutions of 0.1445 (MG 0414+0534), 0.1618 (RXJ 0911+0551), 0.2207 (B 1422+231), and 0.1341 (WFI J2026-4536) light-days. This resolution is ∼0.5 times the innermost stable circular orbit of a $10^9 M_\odot$ black hole, sufficient for our rest-frame UV to optical observations.

All physical sizes quoted in this paper depend on the choice of microlens mass M_{micro}, so all physical units can be rescaled by a factor of $(M_{micro}/M_\odot)^{1/2}$. We omit this factor from scales throughout this paper for readability, but it should be assumed to be present in every physical measurement obtained via microlensing simulations.

All magnification maps are available for download via the GER-LUMPH website.[2]

4.2.2 Isolating the microlensing signal

We conduct our microlensing simulations using the magnitude differences $\Delta m_{obs} = m_B - m_A$ (or $m_{A_2} - m_{A_1}$ as appropriate) provided in Table 3. We note that the simulations can trivially be run in terms of flux ratio instead, as in our previous papers (Bate et al. 2008; Floyd et al. 2009), using the relationship $\Delta m_{obs} = m_B - m_A = -2.5\log_{10}(f_B/f_A)$.

In an ideal case, we would isolate the microlensing signal from both macrolensing and differential extinction by using a series of Δm measurements from emission regions in the source large enough to be unaffected by microlensing. These emission regions would need to emit at similar wavelengths to the continuum source in order to accurately map the effects of extinction.

The procedure adopted by Mediavilla et al. (2009) and following papers were to use the centres of broad emission lines in spectra to establish unmicrolensed baselines. We do not currently have access to suitable spectra for all of our systems, and in any case there is some question over the accuracy of the assumption that no microlensing is present in the centres of broad emission lines.

We chose instead to normalize all of our observed magnitude differences within a given system to a single unmicrolensed baseline: $\Delta m_{micro} = \Delta m_{obs} - \Delta m_{macro}$. The baseline Δm_{macro} is taken in the radio or infrared where possible, and removes only the effects of macrolensing. This is the second key difference between our analysis and JV14. In practice, it means that we are attributing all of the chromatic variation in our observations to microlensing, and none

---

[2]http://gerlumph.swin.edu.au

Table 2. Observed Vega magnitudes of all lensed images and lensing galaxies.

Object	Filter								
	F410M	F547M	F621M	F689M	F763M	F845M	F105W	F125W	F160W
MG 0414+0534									
Image A_1	—	—	—	—	15.69 ± 0.05	14.05 ± 0.03	—	16.60 ± 0.01	15.52 ± 0.01
Image A_2	—	—	—	—	16.86 ± 0.09	14.98 ± 0.05	—	17.04 ± 0.02	15.81 ± 0.01
Image B	—	—	—	—	16.38 ± 0.07	14.79 ± 0.05	—	17.55 ± 0.02	16.51 ± 0.02
Image C	—	—	—	—	17.24 ± 0.11	15.66 ± 0.07	—	18.38 ± 0.03	17.31 ± 0.02
Lens galaxy	—	—	—	—	[a]	[a]	—	19.00 ± 0.03	18.26 ± 0.04
RXJ 0911+0551									
Image A	—	16.32 ± 0.03	16.00 ± 0.04	15.80 ± 0.04	—	15.69 ± 0.09	—	18.70 ± 0.04	18.41 ± 0.05
Image B	—	15.75 ± 0.02	15.46 ± 0.03	15.22 ± 0.03	—	15.08 ± 0.05	—	18.15 ± 0.03	17.87 ± 0.03
Image C	—	16.69 ± 0.04	16.37 ± 0.05	16.14 ± 0.05	—	15.99 ± 0.07	—	18.93 ± 0.04	18.63 ± 0.05
Image D	—	16.95 ± 0.05	16.60 ± 0.06	16.39 ± 0.06	—	16.29 ± 0.14	—	19.28 ± 0.04	18.98 ± 0.05
Lens galaxy	—	[a]	[a]	[a]	—	[a]	—	18.45 ± 0.21	17.77 ± 0.32
B 1422+231									
Image A	—	—	10.86 ± 0.01	—	10.14 ± 0.01	9.58 ± 0.01	15.47 ± 0.01	14.95 ± 0.02	14.50 ± 0.01
Image B	—	—	11.35 ± 0.01	—	10.59 ± 0.01	9.98 ± 0.01	15.74 ± 0.01	15.12 ± 0.02	14.61 ± 0.01
Image C	—	—	11.43 ± 0.01	—	10.69 ± 0.01	10.13 ± 0.01	16.01 ± 0.01	15.53 ± 0.02	15.07 ± 0.01
Image D	—	—	14.56 ± 0.03	—	13.79 ± 0.03	13.22 ± 0.04	19.00 ± 0.04	18.45 ± 0.11	17.88 ± 0.05
Lens galaxy	—	[a]	[a]	—	[a]	[a]	19.23 ± 0.05	18.71 ± 0.09	18.11 ± 0.08
WFI J2026−4536									
Image A_1	15.21 ± 0.03	15.04 ± 0.02	—	14.38 ± 0.02	14.06 ± 0.02	13.83 ± 0.03	—	16.32 ± 0.01	15.76 ± 0.01
Image A_2	14.29 ± 0.02	14.78 ± 0.02	—	14.37 ± 0.02	14.13 ± 0.02	13.95 ± 0.03	—	16.60 ± 0.01	16.14 ± 0.02
Image B	15.57 ± 0.04	16.01 ± 0.03	—	15.56 ± 0.04	15.28 ± 0.03	15.09 ± 0.06	—	17.74 ± 0.04	17.20 ± 0.04
Image C	15.72 ± 0.05	16.17 ± 0.04	—	15.75 ± 0.05	15.49 ± 0.04	15.32 ± 0.07	—	17.92 ± 0.04	17.46 ± 0.04
Lens galaxy	[a]	[a]	—	[a]	[a]	[a]	—	19.92 ± 0.29	18.62 ± 0.11

[a]Not detected in our data.

Table 3. Observed magnitude differences used in the current microlensing analysis.

System	Images	Observed wavelength (Å)								
		4109	5447	6219	6876	7612	8436	10552	12486	15369
MG 0414+0534	A_2–A_1	–	–	–	–	1.17 ± 0.11	0.93 ± 0.06	–	0.44 ± 0.02	0.29 ± 0.01
RXJ 0911+0551	B–A	–	−0.57 ± 0.04	−0.54 ± 0.05	−0.58 ± 0.05	–	−0.61 ± 0.10	–	−0.55 ± 0.05	−0.54 ± 0.06
B 1422+231	B–A	–	–	0.49 ± 0.01	–	0.45 ± 0.01	0.40 ± 0.01	0.27 ± 0.01	0.17 ± 0.02	0.11 ± 0.01
WFI J2026-4536	A_2–A_1	−0.92 ± 0.03	−0.26 ± 0.02	–	−0.01 ± 0.03	0.07 ± 0.02	0.12 ± 0.04	–	0.28 ± 0.02	0.38 ± 0.02

to any other chromatic effects such as differential extinction. We note that since extinction can effect either image in a lensed pair, neglecting differential extinction could lead us to overestimate *or* underestimate the size of any chromatic microlensing.

The literature data used to determine unmicrolensed baselines are provided in Table 6. We can compare the observed baselines with the predictions from our lens models, to check for consistency. In two cases, MG 0414+0534 and B 1422+231, we find that our lens model values lie marginally outside the observed values. To account for this, we expand the errors on the unmicrolensed baselines used in our simulations. We do not have suitable observations for WFI J2026-4536, so we choose to assume that the lens model prediction for the unmicrolensed baseline is correct, but assign it a correspondingly large error (23 percent in the ratio). This value for the error was chosen conservatively: it is approximately twice the percentage error in the least-accurately measured unmicrolensed baseline in our sample (RXJ 0911+0551), and approximately twice the largest deviation between model predicted and observed values (B 1422+231).

In Table 7, we provide the measured microlensing amplitudes $\Delta m_{\mathrm{micro}} = \Delta m_{\mathrm{obs}} - \Delta m_{\mathrm{macro}}$ for each of our four systems. Here, we have simply added the errors in the unmicrolensed baseline (Table 6, fifth column) to the observational errors in quadrature. We note that these errors are handled differently in our microlensing simulations, as they represent a systematic offset rather than an independent error in each data point. This will be described in detail in the next section. Table 7 is provided to give a sense of the size of the microlensing signal in each system.

4.2.3 Microlensing simulations

We use a Bayesian analysis to constrain the size of the quasar accretion disc r_s at $\lambda_0 = 1026$Å, and the power-law index p. The radial profile of the accretion disc is assumed to be of the form

$$r = r_s \left(\frac{\lambda}{\lambda_0} \right)^p . \tag{1}$$

We use Gaussian profiles to describe the shape of the disc at each wavelength; the measured sizes r_s are Gaussian dispersions. Mortonson, Schechter & Wambsganss (2005) have demonstrated that size estimates from microlensing simulations are independent of the detailed surface brightness profile shapes, but rather depend only on the characteristic width of that profile.

Following JV14, we vary parameters on a regular grid, such that $ln(r_s) = 0.3 \times j$ for $j = 0 \ldots 11$, and $p = 0.25 \times i$ for $i = 0 \ldots 15$. This is a slightly larger range in p than in JV14.

For each combination of $ln(r_s)$, p, and s, the magnification maps for image 1 and image 2 are convolved with a series of Gaussian source profiles with dispersion r calculated at the rest-frame wavelengths of the observations using equation (1). Each map is then sampled on a regular grid of 10^4 points. This allows us to construct 10^8 simulated magnification ratios per $ln(r_s)$-p-s parameter combination for comparison with the observational data. We note that we sample only from the central 2000 × 2000 pixel area of each magnification map; 10 000 × 10 000 pixel maps allow us to convolve with large source profiles while avoiding convolution edge effects. The effective upper limit on our simulated source sizes is 8 Einstein radii.

Errors in the unmicrolensed baseline affect observed flux ratios at each wavelength equivalently: they simply act as a systematic offset. To account for this, we include the unmicrolensed baseline $\Delta m_{\mathrm{macro}}$ as a nuisance parameter in our Bayesian analysis. At each of the 10^8

Table 4. Microlensing parameters, convergence κ, and shear γ.

System	Image	κ	γ	Image	κ	γ	Source
MG 0414+0534	A_1	0.51	0.42	A_2	0.56	0.51	MacLeod et al. (2013)
RXJ 0911+0551	A	0.65	0.54	B	0.59	0.28	Schechter et al. (2014)
B 1422+231	A	0.38	0.47	B	0.49	0.63	Schechter et al. (2014)
WFI J2026-4536	A_1	0.52	0.40	A_2	0.54	0.54	This work

Table 5. Table 5. Lens model parameters.

Object	Primary lens			Shear		Secondary lens			Tertiary lens			Source
	θ_{Ein}	e	ϕ_e	γ	ϕ_γ	b_2	x_2	y_2	b_3	x_3	y_3	
MG 0414+0534	$1''084$	0.238	-83.9	0.094	53.1	$0''176$	$0''857$	$0''181$	$0''007$	$-0''97$	$-1''39$	MacLeod et al. (2013)
RXJ 0911+0551	$0''95$	0.11	-70.0	0.294	8.3	$0''22$	$-0''754$	$0''665$	–	–	–	Schechter et al. (2014)
B 1422+231	$0''74$	0.39	-58.9	0.137	-47.2	–	–	–	–	–	–	Schechter et al. (2014)
WFI J2026-4536	$0''651$	0.133	-25.0	0.133	82.9	–	–	–	–	–	–	This work

Table 6. Unmicrolensed baselines Δm_{macro}.

System	Image pair	Observed	Lens model	Adopted	Observed wavelength
MG 0414+0534	A_2–A_1	0.09 ± 0.02	0.04	0.09 ± 0.05	11.7 μm (Minezaki et al. 2009); 11.2 μm (MacLeod et al. 2013)
RXJ 0911+0551	B–A	-0.74 ± 0.10	-0.69	-0.74 ± 0.10	5 GHz (Jackson et al. 2015)
B 1422+231	B–A	-0.08 ± 0.02	-0.20	-0.08 ± 0.12	8.4 GHz (Patnaik et al. 1999)
WFI J2026-4536	A_2–A_1	–	0.14	0.14 ± 0.25	–

simulated observations, we re-sample Δm_{macro} from a Gaussian with mean and dispersion equal to the observed unmicrolensed baseline and its error (see Table 6), and re-normalize the observed data. This effectively marginalizes over errors in the unmicrolensed baseline.

We note that this differs from the usual technique (e.g. JV14), where the error in the unmicrolensed baseline is simply added into the observed errors in quadrature. This is equivalent to assuming that errors in the baseline affect each wavelength independently, rather than systematically.

We construct likelihoods $\mathcal{L}_k$ for each simulated observation k using a χ^2 comparison:

$$\mathcal{L}_k(\Delta m_{\text{micro}}|ln(r_s), p, s) = \exp\left(\frac{-\chi_k^2}{2}\right). \quad (2)$$

The final likelihood for a given combination of parameters $ln(r_s)$, p, s is simply the sum over all of the likelihoods of the individual simulated observations $\mathcal{L} = \sum_k \mathcal{L}_k$.

Differential probability distributions are generated from the likelihoods using Bayes' theorem:

$$\frac{d^3P}{dln(r_s)dpds} \propto \mathcal{L}(\Delta m_{\text{micro}}|ln(r_s), p, s)\frac{dP_{\text{prior}}}{dln(r_s)}\frac{dP_{\text{prior}}}{dp}\frac{dP_{\text{prior}}}{ds}. \quad (3)$$

We use flat priors for all three parameters (equivalent to a logarithmic prior on the source size r_s). Since we are interested in the quasar accretion discs, we integrate over ds as a nuisance parameter. Results are presented as mean values with 68 per cent confidence intervals, or 68 per cent upper/lower limits where appropriate.

5 RESULTS

Probability distributions for the accretion disc parameters in each of our four systems are provided in Fig. 2, marginalized over the smooth matter fraction and errors in the unmicrolensed baseline. In each figure we have marked the power-law index of an SS disc with

a dashed red line ($p = 4/3$), and the Bayesian ensemble estimate from JV14 with a hashed region ($p = 0.8 \pm 0.2$).

The dotted light blue line in each figure marks the point at which the combination of parameters $ln(r_s)$ and p gives a source size in the reddest filter that is larger than we can fit in our 100 Einstein radius maps (this limit is a Gaussian dispersion of 8 Einstein radii). Beyond this point, we simply assume that the simulated flux ratio equals the unmicrolensed macroflux ratio. In most cases this is a reasonable assumption, however large-scale structures in sheared magnification maps (conglomerations of caustics stacked on top of each other) can still cause slight deviation from the macroflux ratio, even at these sizes.

Although there may be some probability that the true accretion disc parameters lie beyond this dotted light blue line (specifically in MG 0414+0534 and WFI J2026-4536), we do not expect it to be significant. In any case, if we expanded the maximum size limitations in our simulations the measured p constraints could only skew to higher values, pushing them further away from the JV14 result.

The formal 68 per cent constraints obtained from these probability distributions are provided in Table 8. We quote results after marginalizing over the smooth matter fraction s, as well as the constraints obtained if we assume $s = 0.8$. The most notable feature of these measurements and the probability distributions in Fig. 2 is their diversity, particularly when compared with JV14 or Blackburne et al. (2011). The reasons for these differences will be discussed in the following section.

We show the explicit dependence of our accretion disc constraints on the assumed smooth matter fraction s in Fig. 3 (RXJ 0911+0551 is excluded from this figure; the data for this system do not provide constraints at any smooth matter fraction). With a few exceptions, we obtain only upper limits on the size r_s of the accretion disc at $\lambda_0 = 1026$Å (in B 1422+231 we obtain a measurement, but its error bars are large). For the power-law index p, we find the marginalized

Table 7. Observed microlensing amplitudes, defined as $\Delta m_{\mathrm{micro}} = \Delta m_{\mathrm{obs}} - \Delta m_{\mathrm{macro}}$.

System	Images	$\Delta m_{\mathrm{macro}}$	Observed wavelength (Å)								
			4109	5447	6219	6876	7612	8436	10552	12486	15369
MG 0414+0534	A2–A1	0.09 ± 005^a	–	–	–	–	1.08 ± 0.12	0.84 ± 0.08	–	0.35 ± 0.05	0.20 ± 0.05
RXJ 0911+0551	B–A	-0.74 ± 0.10^b	–	0.17 ± 0.11	0.20 ± 0.11	0.16 ± 0.11	–	0.13 ± 0.14	–	0.19 ± 0.11	0.20 ± 0.12
B 1422+231	B–A	-0.08 ± 0.12^c	–	–	0.57 ± 0.12	–	0.53 ± 0.12	0.48 ± 0.12	0.35 ± 0.12	0.25 ± 0.12	0.19 ± 0.12
WFI J2026-4536	A2–A1	0.14 ± 0.25^d	-1.06 ± 0.25	-0.40 ± 0.25	–	-0.15 ± 0.25	-0.08 ± 0.25	-0.03 ± 0.25	–	0.14 ± 0.25	0.24 ± 0.25

[a] Minezaki et al. (2009); MacLeod et al. (2013).
[b] Jackson et al. (2015).
[c] Patnaik et al. (1999).
[d] Obtained from macromodelling, rather than from observed IR or radio data. Errors in $\Delta m_{\mathrm{macro}}$ added to observed errors in quadrature (see Sections 4.2.2 and 4.2.3).

constraints are completely consistent with each of the individual smooth matter cases, tending to deviate only at $s = 0.99$. There is a slight trend towards decreasing p (steepening temperature profile) with increasing s, most pronounced in MG 0414+0534.

For the remainder of this paper, we restrict ourselves to discussing results for the $s = 0.8$ case. We choose this value following Jiménez-Vicente et al. (2015a), who measured $s = 0.79 \pm 0.14$ from a sample of 19 lensed quasars. We note, however, that this specific constraint is not uniformly applied in the literature: for example, Rojas et al. (2014) and Motta et al. (2017) use $s = 0.9$, and JV14 used $s = 0.95$.

6 DISCUSSION

6.1 Accretion disc size r_s

The accretion disc sizes quoted in Table 8 are Gaussian dispersions, assuming $1 M_\odot$ microlenses. To facilitate comparisons with thin-disc theory, we convert to half-light radii $r_{1/2} = 1.18\, r_s$. The average stellar microlens in a lensing galaxy is likely to be less massive than $1 M_\odot$; the standard value used is $M_{\mathrm{micro}} = 0.3 M_\odot$, which enters into our source sizes as a factor of $(M_{\mathrm{micro}}/M_\odot)^{1/2}$. Our resulting half-light radius measurements assuming $0.3 M_\odot$ microlenses are provided in Table 9.

The half-light radius of a standard thin disc (Shakura & Sunyaev 1973) is

$$r_{\mathrm{thin}} = 2.44 \left(\frac{45 G^2 M_{\mathrm{BH}}^2 m_p f_{\mathrm{Edd}} \lambda^4}{4\pi^5 h_p c^3 \sigma_T \eta} \right)^{1/3} \sqrt{\cos i}$$

$$= 6.49\mathrm{ld} \left(\frac{M_{\mathrm{BH}}}{10^9 M_\odot} \right)^{2/3} \left(\frac{f_{\mathrm{Edd}}}{\eta} \right)^{1/3} \left(\frac{\lambda}{\mu\mathrm{m}} \right)^{4/3}, \quad (4)$$

where M_{BH} is the black hole mass, m_p is the proton mass, h_p is Planck's constant, σ_T is the Thomson scattering cross-section, and i is the inclination angle (assumed to be $\langle \cos i \rangle = 1/2$). f_{Edd} is the Eddington ratio, the ratio of the quasar's bolometric luminosity to the Eddington luminosity, and η is the accretion efficiency. Finally, λ is the rest wavelength of interest.

Black hole mass measurements are available for three of our systems: MG 0414+0534, RXJ 0911+0551, and B 1422+231(Mosquera & Kochanek 2011). For WFI J2026-4536, we assume a fiducial $M_{\mathrm{BH}} = 10^9 M_\odot$. In Table 9, we provide black hole masses and ratios of measured half-light radius $r_{1/2}$ to the thin disc prediction r_{nthin}, calculated using equation (4).

For MG 0414+0534and WFI J2026-4536, our two systems showing the largest chromatic variation, we obtain only upper limits. Nevertheless, in line with previous microlensing analyses, we find that our measured sizes are consistent with being larger than expected from thin disc theory (only marginally, in the case of MG 0414+0534). In JV14, they quoted an ensemble measurement of $r_s = 4.5^{+1.5}_{-1.2}$ light-days for eight quasars (assuming $1 M_\odot$ microlenses). Converting that to half-light radius as described above, their constraint is $r_{1/2} = 2.9^{+1.0}_{-0.8}$ light-days. This is marginally larger than our measurement for MG 0414+0534, and completely consistent with our B 1422+231and WFI J2026-4536results.

6.2 Power-law index p

In JV14, the authors report a Bayesian estimate of the power-law index p of 0.8 ± 0.2, measured jointly from eight lensed quasars. The accretion disc temperature profile goes as $T \propto r^{-1/p}$, so this corresponds to a steeper temperature profile than expected for an SS disc.
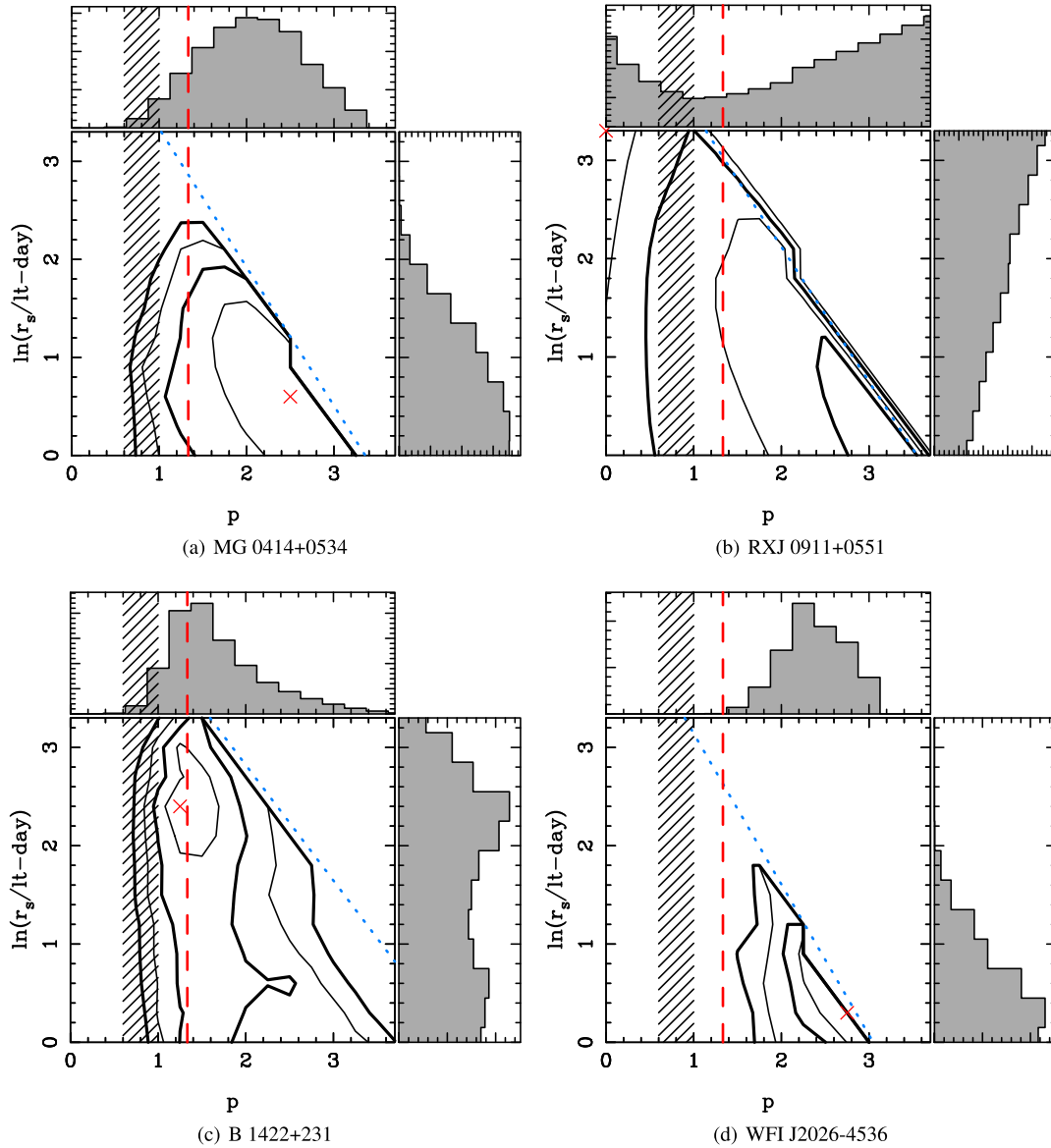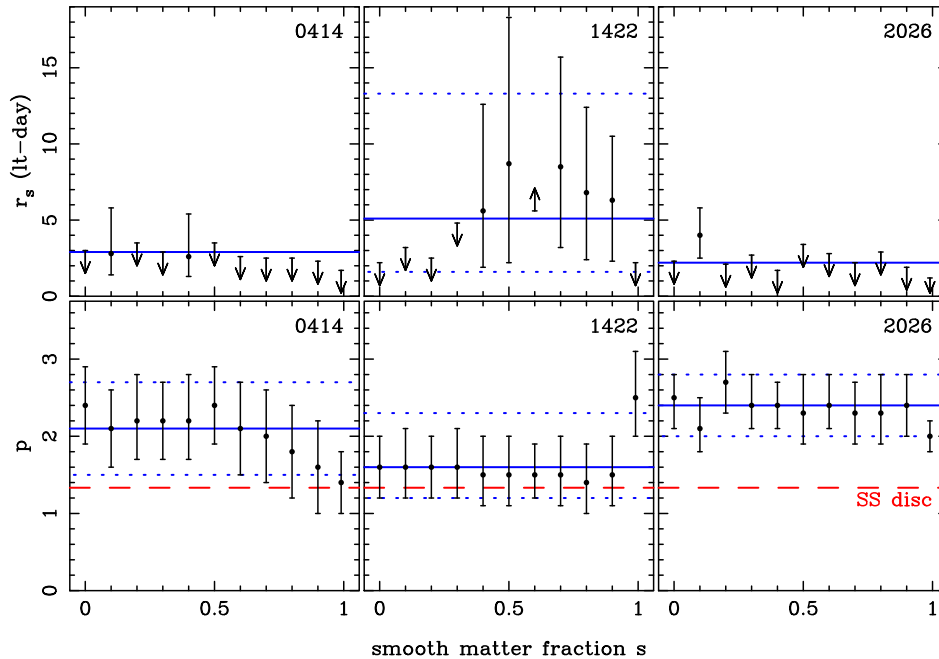
Figure 2. Accretion disc constraints for four lensed quasars using our *HST* data only. Contours are drawn at intervals of 0.5σ (thick lines at 1σ and 2σ) for two degrees of freedom from the maximum. The solid contours therefore formally contain 68.3 and 95.4 per cent of the probability. The dashed red line marks the power-law index for the SS disc (Shakura & Sunyaev 1973). The hatched region is the joint 1σ constraint from JV14. The red cross marks the peak probability in the two-dimensional surface, and the dotted light blue line is the limit of our simulations (see Section 5). Panel (a): MG 0414+0534. Panel (b): RXJ 0911+0551. Panel (c): B 1422+231. Panel (d): WFI J2026-4536.

Table 8. Measured accretion disc constraints (68 per cent).

System	Marginalized		80 per cent smooth matter	
	r_s (light-day)	p	r_s (light-day)	p
MG 0414+0534	<2.9	$2.1^{+0.6}_{-0.6}$	<2.5	$1.8^{+0.6}_{-0.6}$
RXJ 0911+0551	–	–	–	–
B 1422+231	$5.1^{+8.2}_{-3.5}$	$1.6^{+0.7}_{-0.4}$	$6.8^{+5.6}_{-4.4}$	$1.4^{+0.5}_{-0.4}$
WFI J2026-4536	<2.2	$2.4^{+0.4}_{-0.4}$	<2.9	$2.3^{+0.5}_{-0.4}$

This steep temperature profile measurement is difficult to understand in the context of microlensing light-curve constraints on accretion disc sizes (e.g. Morgan et al. 2010), or recent reverberation mapping experiments (e.g. Jiang et al. 2017; Starkey et al. 2017),

which consistently measure accretion discs to be factors of ∼4 larger than expected from thin disc theory. Naively, you would expect that larger accretion discs at a given wavelength imply shallower temperature profiles.

Figure 3. Variation of accretion disc constraints as a function of smooth matter fraction s. Error bars denote 68 per cent confidence. Arrows are 68 per cent upper limits ($s = 0.6$ in B 1422+231 is a lower limit). The top panels show size constraints r_s. The bottom panels show constraints on the temperature profile power-law index p. Blue lines indicate the constraints obtained when marginalizing over s. In the top left (MG 0414+0534) and top right (WFI J2026-4536) panels, these are 68 per cent upper limits. In all other panels, the solid blue lines show the marginalized constraint, and the dotted blue lines the 68 per cent confidence limits. The Shakura-Sunyaev power-law index $p = 4/3$ is plotted as a dashed red line in the bottom panels.

Table 9. Measured accretion disc half-light radii (68 per cent).

System	$r_{1/2}$ (light-day)	M_{BH} ($10^9 M_{\odot}$)^a	$r_{1/2}/r_{nthin}$
MG 0414+0534	<1.6	1.82	<1.6
RXJ 0911+0551	–	0.80	–
B 1422+231	$4.4^{+3.6}_{-2.8}$	4.79	$2.3^{+1.9}_{-1.5}$
WFI J2026-4536	<1.9	1.00^b	<2.8

Notes: Results assuming smooth matter fraction $s = 0.8$.
^{a} From Mosquera & Kochanek (2011).
^{b} Fiducial value; no measured black hole mass available.

We have measured p in four additional systems, and we prefer *larger* values of p than 4/3 in two of our systems: WFI J2026-4536 and MG 0414+0534 (marginally). Both of these results are consistent with the $p = 2.0$ slim disc prescription of Abramowicz et al. (1988). In the third system, B 1422+231, we find $p \sim 4/3$ is preferred, consistent with standard SS thin discs. Our RXJ 0911+0551 data are insufficient to place any constraints on its accretion disc structure.

Why do we find such a variety of constraints on p, where the measurements in JV14 were largely consistent with each other, converging on $p = 0.8 \pm 0.2$? In Fig. 4, we plot all of the observations reported in JV14 (black triangles, from their Table 1) and this paper (red circles). The figure shows absolute magnitude differences between lensed images as a function of rest wavelength in each quasar. The variation in absolute magnitude difference between shortest and longest wavelength represents the degree of microlensing-induced chromatic variation in each system.

Fig. 4 clearly illustrates that two of our systems – MG 0414+0534 and WFI J2026-4536 – display more chromatic variation than any of the objects studied in JV14. In contrast, B 1422+231 shows chromatic microlensing effects broadly similar to the JV14 sample,

and RXJ 0911+0551 has essentially no chromatic microlensing at all. Note that there is no overlap between the systems studied here, and those in JV14.

In cases where we observe strong chromatic effects, we find $p > 4/3$, whereas in cases where chromatic effects are weaker we find p consistent with (or even smaller than) 4/3. If we look at the individual quasars in the JV14 sample, two of the three systems displaying the strongest chromatic effects also provide the largest estimates of the power-law index (HE 0512-3329: maximum likelihood $p = 1.25^{+0.6}_{-0.7}$, Bayesian $p = 1.4 \pm 0.6$; SDSS J1004+4112: maximum likelihood $p = 1.00^{+1.00}_{-0.5}$, Bayesian $p = 1.3 \pm 0.6$). This trend is illustrated in Fig. 5, where we plot the observational constraints for each system in JV14 (black) and this work (red) as a function of the size of their chromatic variation. The latter is defined as $\Delta m_{max} - \Delta m_{min}$ (usually, but not always, the bluest observation minus the reddest). The error bars in the individual observations are large; formally, they are all consistent with each other, and with the SS disc prediction. Nevertheless, there does appear to be a general trend, as described above: observations with lower chromatic variation tend to predict lower values of p.
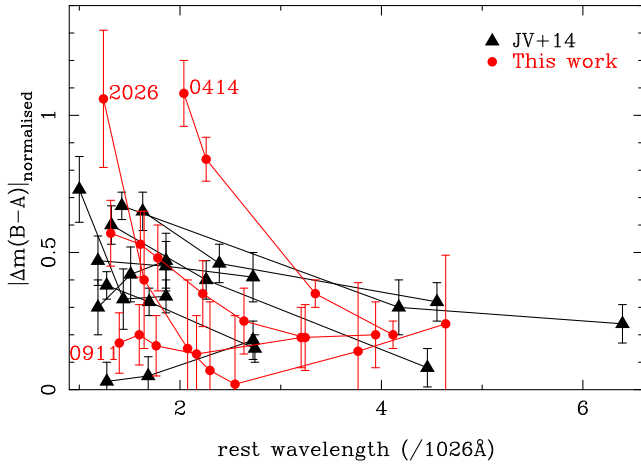
Figure 4. Absolute values of observed magnitude differences between lensed images, normalized to their expected macromagnifications (errors in our *HST* data are largely dominated by errors in the expected macromagnifications; see Tables 3 and 7). The red circles are four sets of observations reported in this paper, whereas the black triangles are the sample from JV14 (excluding Q 2237+0305, the data for which were not provided in that paper). $B - A$ is adopted for labelling convenience; in MG 0414+0534 and WFI J2026-4536, $A = A_1$ and $B = A_2$. The label for B 1422+231 is omitted from the plot for clarity. It is clear from this figure that MG 0414+0534 and WFI J2026-4536 show a much greater degree of chromatic variation than any of the systems in the JV14 sample.
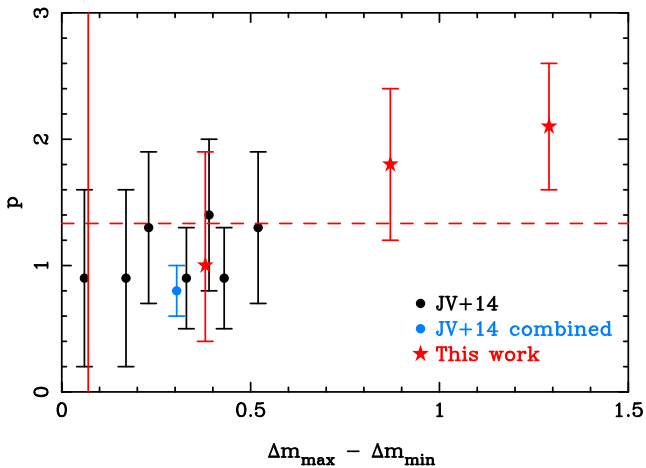
Figure 5. Power-law constraints p (68 per cent confidence) as a function of the size of chromatic variation in the observation. As the degree of chromatic variation increases, so does the measured constraint on the power-law index. Seven quasars are presented from Jiménez-Vicente et al. (2014) (filled black circles, Bayesian constraints), along with their joint constraint at the average chromatic variation of their sample (light blue filled circle). Three quasars from this work are shown (red stars, $s = 0.80$), with a vertical red line marking the degree of chromatic variation in the fourth (RXJ 0911+0551, where we obtain no constraint). The red dashed line marks the power-law index $p = 4/3$, appropriate for the standard SS disc.

Assuming this trend is real, is it due to the physical situation in each individual quasar? Do the quasars where we observe lower chromatic variation actually have steeper temperature profiles in their accretion discs? Or is it simply a (misleading) selection effect, where observations with low chromatic variation lead us to believe we are observing a steeper temperature profile than actually exists in the quasar? We can check this with mock simulations, where

we test how well we are able to recover a known input accretion disc using our single-epoch microlensing analysis technique. We analyse a sample suite of mock simulations below.

7 MOCK OBSERVATIONS

To explore whether the correlation between size of the observed chromatic variation and the slope of the measured temperature profile is real or simply a selection effect, we generated a suite of 200 mock observations for a single input accretion disc. These were conducted in a blind fashion – one of us (GV) produced the mock data, and provided it as a set of magnitude differences to another (NFB), who ran them through the microlensing analysis pipeline. The purpose of these mock observations was twofold: (1) to test whether observations with low chromatic variation produce accretion disc constraints biased towards low p, and (2) to test whether any observations recover the input disc parameters.

7.1 Mock observation technique

The same machinery was used to produce the mock observations as described in Section 4.2. We used equation (1) to create a series of Gaussian profiles to describe the shape of the accretion disc for each observed wavelength in Table 3, with the parameters $p = 1.5$ and $r_s = 2.7$ light-days. We did this using the MG 0414+0534 macro-model, and the magnification maps we have already generated. For simplicity, we assumed the magnification for image A_1 to be constant and equal to the macromagnification. We then selected a map with a fixed s for image A_2, convolved it with the generated source profiles, and sampled magnification values from the central 6700×6700 pixel area. This area was chosen in order to avoid convolution edge effects; the largest source profile, for observed wavelength $\lambda = 15369$ Å, corresponds to roughly 3300 pixels in the source plane.

We used $s = 0.8$ and $s = 0.9$ magnification maps to generate the mock data, drawing 100 mock observations from each map. These smooth matter fractions are consistent with the values we expect to find in a real MG 0414+0534-like quasar. Using two smooth matter fractions allowed us to generate more statistically independent mock observations, and also to test whether the choice of s had an effect on our results. Unsurprisingly, we found that it did not – the two cases were indistinguishable.

Throughout, we have assumed errors on our mock observations of ±0.05 in the UVIS channel, and ±0.02 in the IR channel. These are consistent with our *HST* observations. Although simulated magnitude differences were generated for nine *HST* filters (see Table 1), we used only five for the microlensing analysis: F410M (4109Å), F621M (6219Å), F845M (8436Å), F125W (12486Å), and F160W (15369Å).

7.2 Mock observation results

The results of single-epoch microlensing analysis on our mock observations are presented in Figs 6 (source size r_s) and 7 (power-law index p), plotted as a function of chromatic variation $\Delta m_{max} - \Delta m_{min}$. We have chosen to plot only the simulation results where we assumed a smooth matter fraction of $s = 0.8$ in the analysis pipeline; we also ran the microlensing simulations marginalizing over all smooth matter fractions, and found all of the same trends.

The grey points in Figs 6 and 7 show the individual constraints for each of the mock simulations. The error bars on the individual simulations have been excluded for clarity. Errors on any single measurement are broad, corresponding roughly to the sizes of the
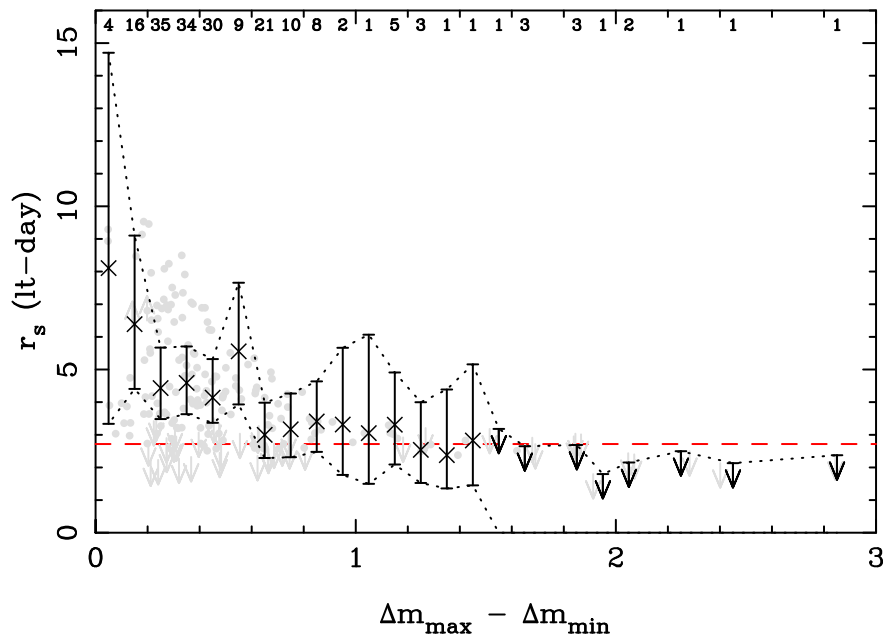
Figure 6. Quasar accretion disc size constraints r_s as a function of the size of chromatic variation in mock observations. Grey points indicate individual measurements for 193 mock observations (error bars excluded for clarity). The dashed red line is the input value of $r_s = 2.7$ light-days. Black crosses are the result of combining all likelihood surfaces in chromatic variation bins with a width of 0.1 (the number of mock observations in each bin is shown across the top of the figure). All error bars are 68 per cent confidence intervals; arrows indicate 68 per cent upper limits.
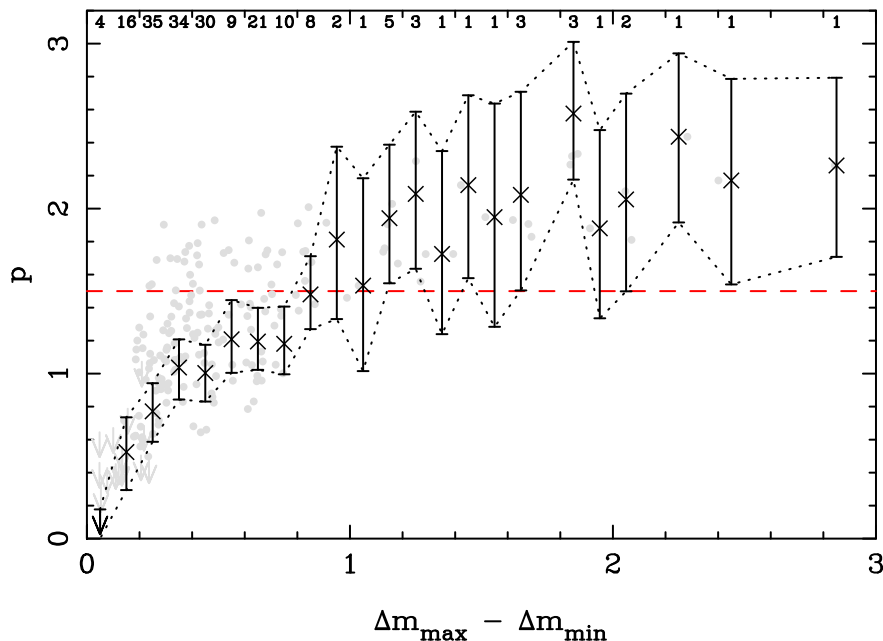
Figure 7. Power-law temperature profile constraints p as a function of the size of chromatic variation in mock observations. Grey points indicate individual measurements for 193 mock observations (error bars excluded for clarity). The dashed red line is the input value of $p = 1.5$. Black crosses are the result of combining all likelihood surfaces in chromatic variation bins with a width of 0.1 (the number of mock observations in each bin is shown across the top of the figure). All error bars are 68 per cent confidence intervals; arrows indicate 68 per cent upper limits.

observed constraints in Fig. 5. A total of 193 points are plotted: seven mock observations returned no meaningful constraints.

We have also combined the likelihood surfaces in bins of $\Delta m_{max} - \Delta m_{min} = 0.1$, treating each mock observation as an independent observation of the same source. These combined results are plotted as black crosses with error bars in Figs 6 and 7; across the top of each plot, we show the number of mock observations in

each bin. Red dashed lines show the input parameters of $r_s = 2.7$ light-days and $p = 1.5$.

These illustrative mock simulations demonstrate exactly the trend seen in the observational data: smaller chromatic variation leads to smaller estimated power-law indices p. They also result in larger estimated source sizes r_s. We note that the simulations presented in Jiménez-Vicente et al. (2014) cover a range in chromatic varia-

tion of roughly $0.04 < \Delta m_{\max} - \Delta m_{\min} < 0.52$. The four quasars presented in this paper span the much larger range from 0.07 (RXJ 0911+0551) to 1.29 (WFI J2026-4536).

Mock observations with chromatic variations larger than $\Delta m_{\max} - \Delta m_{\min} = 1.0$ are rare; in most bins we have only one or a few simulated data points. There is some suggestion that we undershoot (overshoot) the input r_s (p) for sufficiently large chromatic variation, however more mock observations are required to robustly explore this part of parameter space.

Nevertheless, it does appear that for chromatic variation above a certain threshold ($\Delta m_{\max} - \Delta m_{\min} \approx 0.6$) we do recover the input simulation parameters relatively well. We find that we can improve our recovery rate by using only mock observations that roughly converge to the theoretically expected macromagnification in their reddest filter. Using a convergence criterion of $\Delta m_{\mathrm{red}} - \Delta m_{\mathrm{macro}} < 0.3$, we are able to push the threshold of useful data down to chromatic variations of $\Delta m_{\max} - \Delta m_{\min} \approx 0.4$. In Fig. 8, we plot the 110 mock observations that meet this convergence limit.

Fig. 8 clearly shows that in our suite of 200 mock observations, we are able to reliably recover the input value of $p = 1.5$ in ensemble measurements if we restrict ourselves to observations with chromatic variation of $\Delta m_{\max} - \Delta m_{\min} > 0.4$, and convergence to the macromagnification of $\Delta m_{\mathrm{red}} - \Delta m_{\mathrm{macro}} < 0.3$.

7.3 Ensemble measurements

These mock simulations imply that using observations with low chromatic variation leads to systematically underestimating the temperature profile power-law index p. This bias towards smaller p in low chromatic variation observations can be particularly misleading when combining data. We illustrate this in Fig. 9. Here, we have randomly selected eight mock observations and combined their likelihood surfaces to mimic the analysis in JV14 (with the caveat that all of our mock simulations use the same lensing parameters, appropriate for MG 0414+0534, rather than eight separate systems).

In the left-hand panel of Fig. 9, we combine the likelihood surfaces for eight random mock observations that match the range in chromatic variation displayed in JV14 (in that work, $0.04 < \Delta m_{\max} - \Delta m_{\min} < 0.52$; we use $\Delta m_{\max} - \Delta m_{\min} < 0.6$). These combined observations miss the input p (red star) at greater than the 95 per cent level, instead returning a much lower value in line with the JV14 constraint ($p = 0.8 \pm 0.2$). In the middle panel of Fig. 9, we simply combine eight random observations, imposing no constraints. Although the measured r_s and p are marginally closer to the input values in this case, they still undershoot p at greater than the 95 per cent level. This is due to the prevalence of low chromatic variation observations in our mock sample.

In the right-hand panel of Fig. 9, we restrict ourselves to mock simulations meeting the suitability criteria discussed in previous paragraphs ($\Delta m_{\max} - \Delta m_{\min} > 0.4$; $\Delta m_{\mathrm{red}} - \Delta m_{\mathrm{macro}} < 0.3$). Here, we accurately recover the input p, although there is some evidence in this example combination that we still overestimate the size of the accretion disc r_s.

We can make this argument more robust by generating N realizations of eight mock observations each, effectively repeating a JV14-like experiment N times. We can then explore the probability distributions for the recovered r_s and p across the N realizations, using various subsets of the data: completely random, JV14-like (i.e. low chromatic variation), or constrained (i.e. imposing minimum conditions on degree of chromatic variation and convergence to the unmicrolensed baseline).

Given our sample of 200 mock observations, we choose $N = 10$. This gives us sufficient mock data points for statistically independent measurements even when we apply restrictions to our sample.

In Fig. 10, we plot the results of this experiment. The left-hand panel shows the combined probability distribution for accretion disc size r_s of $N = 10$ realizations of eight mock observations each. The right-hand panel shows the distribution for power-law index p. The solid grey histograms are drawn randomly from the full 200 mock observations. The blue hatched histograms represent JV14-like data sets, with $\Delta m_{\max} - \Delta m_{\min} < 0.6$. The red cross-hatched histograms are the result of applying minimum criteria to our mock data: that they display chromatic variation $\Delta m_{\max} - \Delta m_{\min} > 0.4$, and roughly converge to the unmicrolensed baseline as $\Delta m_{\mathrm{red}} - \Delta m_{\mathrm{macro}} < 0.3$.

In all three cases, we systematically overestimate the size of the accretion disc r_s, by a factor of ~ 1.5–2.0. We note that even if selection effects in our data are leading to a factor of 2 overestimation of accretion disc size, the sizes derived from microlensing observations are typically still larger than expected from thin disc theory.

Constraining the mock observations to match the degree of chromatic variation observed in JV14 leads to a systematic underestimation of the power-law index p. In fact, the result we recover here is identical to the JV14 result: 0.8 ± 0.2. If we randomly select instead from the full suite of mock observations, the recovered value of $p = 1.0 \pm 0.2$ shifts slightly closer to the true value, but still predicts a steeper temperature profile at greater than the 2σ level. When we apply constraints on both degree of chromatic variation and convergence to the unmicrolensed baseline, we correctly recover the input value of $p = 1.5$ (formal measured constraint $p = 1.5^{+0.3}_{-0.2}$).

7.4 Comparison with observed data

There are other observations in the literature which use the same technique as JV14 and this paper to constrain quasar accretion discs. It is interesting to see whether they see similar trends. Rojas et al. (2014) presented single-epoch observations (spectra, in this case) of two systems: HE 0047-1756 and SDSS 1155+6346. In both systems, the observed chromatic variation exceeds the rough threshold we find here of $\Delta m_{\max} - \Delta m_{\min} \gtrsim 0.4$. In contrast to JV14, and in line with the general trend observed in this paper, they find $p = 2.3 \pm 0.8$ for HE 0047-1756 (which displays the most chromatic variation) and 1.5 ± 0.6 for SDSS 1155+6346.
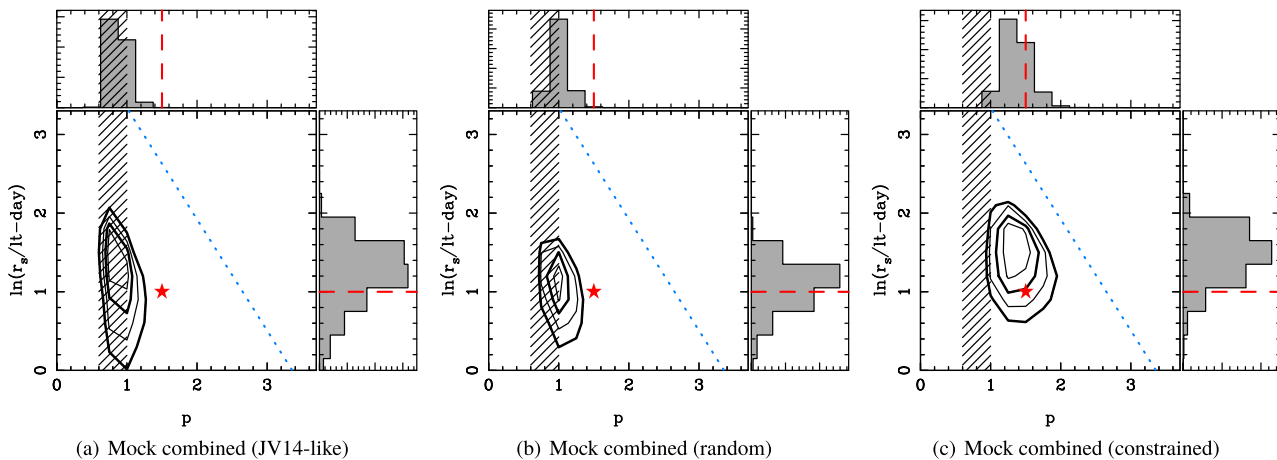
Motta et al. (2017) analysed spectra for three systems: HE 0435-1223, WFI 2033-4723, and HE 2149-2745. Their observed chromatic variations are low: 0.28, 0.26, and 0.11, respectively (the variation in WFI 2033-4723 is the average of four separate epochs of data). As expected, they predict lower values of p. In Fig. 11, we plot all of these observational constraints: our data, JV14, Rojas et al. (2014), and Motta et al. (2017) for r_s and p, along with the binned constraints from our mock observations. We note that these are not technically directly comparable – the observed data are for a range of systems, whereas the mock results are for repeated observations of a single system. Nevertheless, they all follow the same basic trend.

7.5 Mock observation selection effect discussion

We propose here that there are two selection effects that lead to systematically underestimating p in single-epoch microlensing simulations: chromatic variation, and convergence to the unmicrolensed
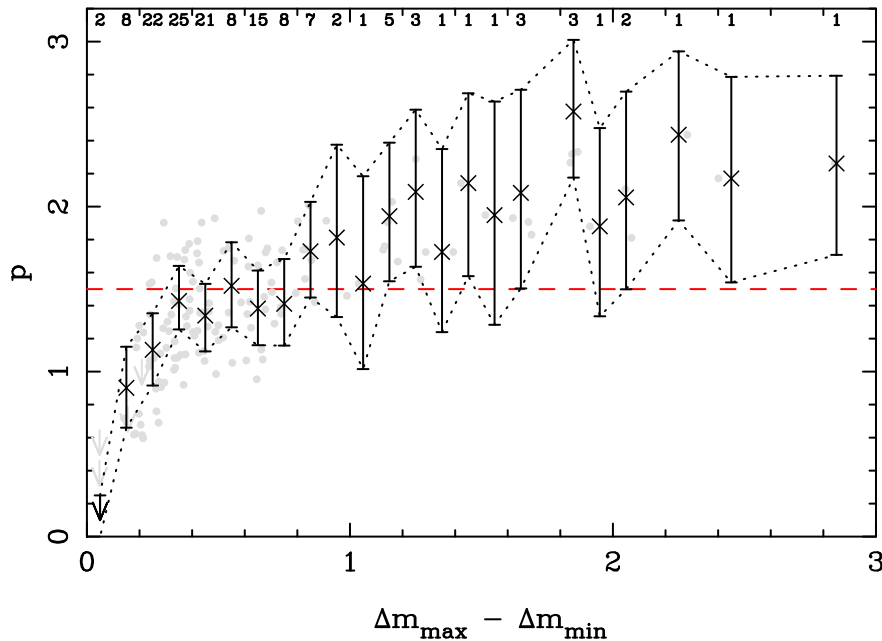
Figure 8. Per Fig. 7, using only mock observations with $|\Delta m_{red} - \Delta m_{macro}| < 0.3$. This leaves 110 mock observations, all of which converge to the unmicrolensed baseline within the applied limit. This cut results in improved recovery of the input power-law index p in the range $\Delta m_{max} - \Delta m_{min} < 1.0$.

(a) Mock combined (JV14-like)   (b) Mock combined (random)   (c) Mock combined (constrained)

Figure 9. Illustrative constraints obtained by combining eight randomly chosen mock observations of an accretion disc with $p = 1.5$, $ln(r_s/\text{light-day}) = 1.0$ (red star and dashed red lines), as per Fig. 2. Panel (a) shows the results when combining observations constrained to match the range of chromatic variation seen in the JV14 data. Panel (b) shows the combination of observations chosen without restriction from our mock data. In Panel (c) we combine mock observations using constraints on chromatic variation and convergence to the unmicrolensed baseline described in Section 7.2.

baseline. Both of these degeneracies are straightforward to understand in the context of convolving a power-law accretion disc model with microlensing magnification maps. When chromatic variations are low, the blue (hotter) and red (colder) parts of the accretion disc are similarly affected by microlensing. Preferred solutions then become accretion disc models where size depends only weakly on wavelength (p is low). It is easier to find positions on the magnification map that produce similar microlensing amplitudes if the relative sizes of the blue and red parts of the accretion disc are similar.

An observed flux ratio in the reddest filter that is significantly offset from the unmicrolensed baseline is easier to produce if the reddest emission region is small. Given that we constrain the accretion disc model to be a power law, if the reddest emission region is

small we have less freedom to choose large values for the power-law index p (due to both the constraints on the resolution of our simulations, and physical limits, i.e. the optical/UV accretion disc cannot extend below the innermost stable orbit).

These findings are related to our earlier observation that small magnitude differences between images provide very little information on the size of the quasar accretion disc (Bate et al. 2007). If we insist that the reddest filter roughly converges to the unmicrolensed baseline, then a low degree of chromatic variation means we are learning almost nothing about the accretion disc (size or temperature profile). If the reddest filter *does not* converge to the unmicrolensed baseline, we may get a tight constraint on size, but p will be artificially driven to low values for the reasons described above.
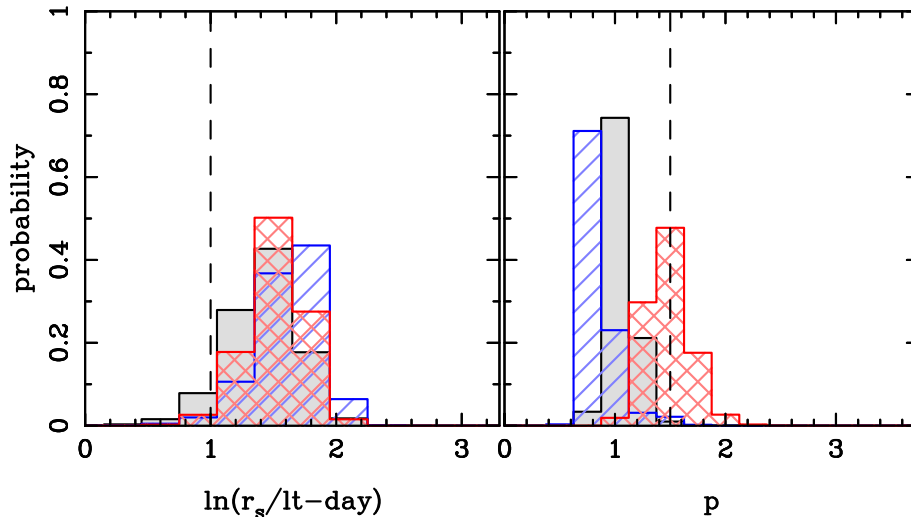
Figure 10. Attempted recovery of input accretion disc parameters (black dashed line) using ten realizations each consisting of eight mock observations drawn from our mock simulation suite. The combined probability distributions are for accretion disc size r_s (left-hand panel) and temperature profile p (right-hand panel). The solid grey histograms represent completely random draws from the full simulation suite. The blue hatched histograms correspond to JV14-like systems, where only low chromatic variation is observed ($\Delta m_{max} - \Delta m_{min} < 0.6$). The red histograms correspond to the case where we apply selection criteria to the data: that a minimum chromatic variation of $\Delta m_{max} - \Delta m_{min} = 0.4$ is observed, and that the observations roughly converge to the unmicrolensed baseline in the reddest filter ($|\Delta m_{red} - \Delta m_{macro}| < 0.3$). Only in this latter case do we correctly recover the input power-law index p; all cases tend to overestimate the accretion disc size.
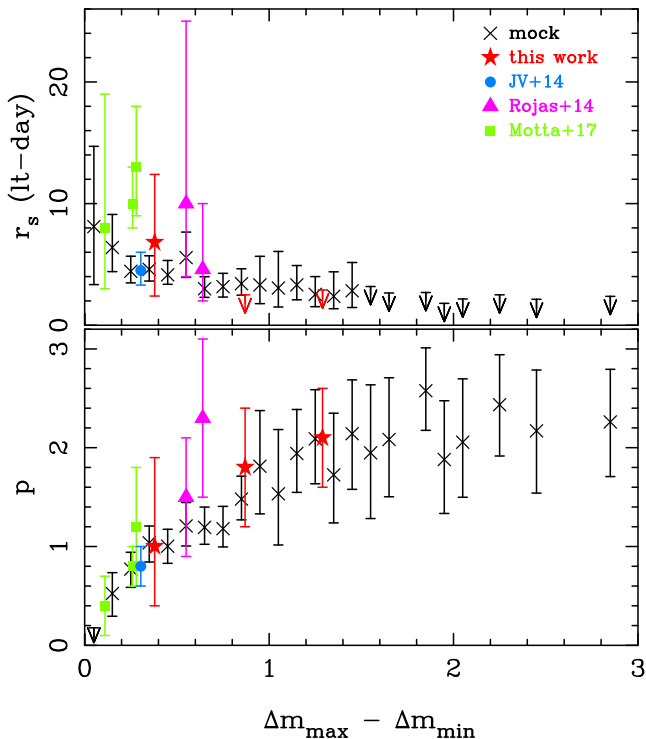
Figure 11. A comparison of mock constraints on r_s (top panel) and p (bottom panel) as a function of chromatic variation, with measurements taken from the literature. Mock data are black crosses, per Figs 6 and 7. Red stars: B 1422+231, MG 0414+0534, WFI J2026-4536 (left to right, this work). Light blue circle: a combination of eight quasars (Jiménez-Vicente et al. 2014). Magenta triangles: HE 0047-1756 and SDSS 1155+6346 (left to right, Rojas et al. 2014). Green squares: HE 2149-2745, WFI 2033-4723 (combination of four independent observations), HE 0435-1223 (left to right, Motta et al. 2017).

7.6 Possible consequences for ensemble measurements

We have demonstrated the selection effects in the previous section for only one simulated accretion disc, with $r_s = 2.7$ light-days and $p = 1.5$. The possible consequences of these effects on real ensemble measurements depend on their generalizability. We discuss the three possible cases below: (a) our results are perfectly general; (b) the trends in our results are general; and (c) our results are not general.

(a) All results are perfectly general

In the case where our results are fully general, the selection effects discussed in the previous section hold for all ensemble single-epoch measurements of accretion disc parameters. We can use the following thresholds to ensure that any ensemble of real observed quasars are providing us with accurate measurements of the underlying disc temperature profile:

(i) $|\Delta m_{red} - \Delta m_{macro}| \lesssim 0.3$, and
(ii) $\Delta m_{max} - \Delta m_{min} \gtrsim 0.4$.

The simplest option for lensed quasar observations that do not meet these requirements is to reject them. If however our results are truly general, then it may be possible to correct for the trends observed in Figs 6 and 7. How to do so in an observed data set, where you have no knowledge of the true accretion disc temperature profile, is not clear.

(b) Only trends are general

In this case, the general trend that low chromatic variation observations lead to underestimating p is true, but the exact shape of the trend depends on some other parameters: perhaps the lens model, or the smooth matter fraction, or the underlying accretion disc temperature profile. In this situation, the thresholds in case (a) might not

be universally applicable – lower chromatic variation observations may be usable in some cases, and misleading in others.

If the shape of these trends depends on external parameters such as the lens model, then we can hopefully account for them by adding a systematic component to our error budgets. If the shape of the trends depends on the underlying accretion disc, the situation is more complicated. Since we have no knowledge of the true temperature profile in a set of real observations, we will not know which of our data are usable. Our best hope in this case is to run suites of mock simulations for various input accretion discs, and determine which ranges of the data return correct results irrespective of the input disc.

Additionally, in this case it becomes crucially important whether high chromatic variation leads to a corresponding *over*-estimation of p. If it does, then any usability thresholds on chromatic variation are likely to be both upper and lower limits; blindly applying a lower limit only might bias us to high p, just as using low chromatic variation biases us towards low p.

(c) Results are not general

We have demonstrated here that low chromatic variation observations do not lead to correct recovery of the input accretion disc for $p = 1.5$. We can imagine, however, that this result is not general – perhaps the single-epoch method correctly measures accretion disc temperature profiles if they are steep (say, $p \sim 1$), but fails to do so if they are shallower (as we have shown for $p = 1.5$). This is the worst-case scenario: given a low chromatic variation observation and no knowledge of the true disc temperature profile, we cannot tell whether our measurement is due to the disc itself or a selection effect.

At this stage, we have no reason to suspect that this case is true. We can think of no *a priori* reason why the method would work well for one mock accretion disc, and fail for another. Nevertheless, our current set of mock simulations do not allow us to rule this case out; we include it here for completeness.

Based on our mock simulations, *in all three cases described above* we must currently doubt the results of any analyses that make use of ensembles of low chromatic variation observations. If cases (a) or (b) are true, we know that such ensembles are likely to underestimate p (although, if case (b) is true, we cannot yet be sure where the cutoff in the usefulness of data occurs). If case (c) is true, we (currently) have no way to differentiate between a situation where the true underlying disc has a steep temperature profile and we are correctly measuring it, or it has a shallow temperature profile and we are underestimating it (as in our mock simulations).

Our analysis for $p = 1.5$ accretion discs only does not provide enough information to discern between cases (a), (b), or (c). To do so, we need a suite of mock observations that covers the full range of astrophysically interesting parameter space: plausible accretion disc temperature profiles, lens models, smooth matter fractions, chromatic variation, and so on. Given the significant computational resources required for such a task, we plan to undertake it in a subsequent paper.

7.7 Additional simulation caveats

In our mock simulations we have made two additional simplifying assumptions: we have used only microlensing parameters appropriate for an MG 0414+0534-like system, and we have assumed that all of the microlensing is in a single image (A_2, the saddle point image). We will discuss some implications of these choices below.

MG 0414+0534 is a high-magnification system ($\mu \sim 25$ in the close image pair), with a high density of caustics in its magnification maps. The models used in JV14 have lensed images with a wide range of magnifications, from $\mu \sim 0.5$ to $\mu \sim 25$. The impact of caustic density on our ability to recover accretion disc parameters with the single-epoch technique has not yet been fully explored. Previous analyses, such as JV14, assume that it makes no difference – that accretion disc parameters are recovered equally-correctly in low and high magnification systems. We take the same position here. This assumption is circumstantially supported by the similarity between the trend in constraints from our mock observations (using only one set of microlensing parameters) and observations in the literature (see Section 7.4 and especially Fig. 11), however it should be more fully tested in the future.

We have also assumed that all of the microlensing is occurring in the saddle point image A_2. It is common in spectroscopic observations of microlensed quasars to find that only one image is strongly affected (see e.g. MacLeod et al. 2015; O'Dowd et al. 2015; Motta et al. 2017), and saddle point images in close image pairs are known to be more strongly effected by microlensing (Schechter & Wambsganss 2002; Vernardos et al. 2014). Nevertheless, by restricting the microlensing to a single image we do exclude some chromatic signatures from our sample of mock observations. In particular, cases where shorter wavelengths in image A_1 are heavily microlensed, leading to an inverted chromatic microlensing curve (this is the case in two of the eight systems presented in JV14).

The mock observations presented here are not intended to be exhaustive. They are, however, all plausible realizations of chromatic microlensing observations in a system like MG 0414+0534; if the standard single-epoch microlensing technique is free of systematic or selection effects, we should recover the input accretion disc parameters correctly. In future work, we will extend our mock observations to cover all of the plausible microlensing parameter space. This will allow us to robustly demonstrate the impact of these selection effects on single-epoch microlensing measurements in a fully realistic sample of lensed quasars.

8 CONCLUSIONS

In this paper, we have presented single-epoch *HST* observations of four gravitationally lensed quasars: MG 0414+0534; RXJ 0911+0551; B 1422+231; and WFI J2026-4536. In each system, we have focussed on close image pairs, where time delays are expected to be negligible. Since we are confident that these images capture the background quasar in the same state, we can use any microlensing-induced chromatic variation to place constraints on the emission regions in the quasar.

Our observations were tuned, as far as was possible, to avoid broad emission lines and therefore provide a clean measurement of microlensing on the quasar accretion discs. Other effects can also masquerade as chromatic microlensing – most notably differential extinction. We have not attempted to isolate these effects; we assume that the entirety of the chromatic variation is due to microlensing.

Using the observed magnitude differences between close image pairs, we place constraints on the size r_s of the quasar accretion disc at $\lambda_0 = 1026\,\text{Å}$ (rest wavelength) and the power-law index p relating accretion disc radius to rest wavelength. We assume an accretion disc spectral profile of the form $r = r_s(\lambda/\lambda_0)^p$. Our simulation technique broadly follows that of JV14, an extension of Bate et al. (2008) and Floyd et al. (2009).

Across our four systems, we find a broad diversity in the measured power-law index p, from $p = 1.4^{+0.5}_{-0.4}$ in B 1422+231, to $p = 2.3^{+0.5}_{-0.4}$

in WFI J2026-4536at 68 per cent confidence (assuming smooth matter fraction $s = 0.8$). This is somewhat at odds with the constraints in JV14, which cluster around $p = 0.8 \pm 0.2$ (their 68 per cent Bayesian constraint obtained by combining observations from eight systems).

There is a trend in our constraints towards larger values of p when the degree of chromatic variation in our observations is greater. To explore the origin of this trend, we generated a suite of 200 blinded mock observations with a known input accretion disc ($r_s = 2.7$ light-days, $p = 1.5$). Accretion disc constraints obtained using the standard single-epoch analysis technique on these mock observations display the following trends:

(i) In cases where the chromatic variation between the bluest and reddest filters in the mock observations is $\Delta m_{\max} - \Delta m_{\min} \lesssim 0.4$, the single-epoch technique systematically underestimates p. Combining multiple mock observations with low chromatic variation in the usual way exacerbates this problem.

(ii) In cases where the mock flux ratio in the reddest filter differs significantly from the unmicrolensed baseline ($|\Delta m_{\mathrm{red}} - \Delta m_{\mathrm{macro}}| \gtrsim 0.3$), the measured p is once again underestimated.

(iii) However, when chromatic variation in the mock observations is sufficiently large, and approximately converges towards the unmicrolensed baseline in the reddest filter, the single-epoch technique correctly recovers input accretion disc power-law index.

This leads to the following important conclusions:

(i) The combined constraint published in Jiménez-Vicente et al. (2014) of $p = 0.8 \pm 0.2$, as well as those in Motta et al. (2017), are likely driven by the low degree of chromatic variation in the ensemble of lensed quasars used in those studies.

(ii) Under the assumption that chromatic variations of $\Delta m_{\max} - \Delta m_{\min} \gtrsim 0.4$ produce clean measurements of the accretion disc temperature profile (implied by our mock observations), we have two systems of interest: MG 0414+0534and WFI J2026-4536. Here, we find very high estimates of p: 1.8 ± 0.6 in MG 0414+0534, $2.3^{+0.5}_{-0.4}$ in WFI J2026-4536 (assuming $s = 0.8$). These correspond to shallower temperature profiles than expected from an SS disc, more in line with Abramowicz et al. (1988) slim discs. If these measurements are accurate, they are consistent with the picture that emerges from both microlensing and reverberation mapping analyses, which generically predict larger accretion discs at a given temperature than expected from SS discs.

We conclude that there are important selection effects that need to be taken into consideration when using the single-epoch microlensing technique to measure accretion disc temperature profiles. First, this technique should be applied to ensembles of quasars – measurements from individual objects have large scatter which does not necessarily reflect anything physical in the source. Secondly, combined results using this technique might be misleading if the chromatic variation is low, or the observations do not roughly converge to the unmicrolensed baseline in the reddest filter. In our mock experiments with $r_s = 2.7$ light-days and $p = 1.5$, we find that the following criteria are sufficient to correctly recover the input values: chromatic variation of $\Delta m_{\max} - \Delta m_{\min} \gtrsim 0.4$, and convergence to the unmicrolensed baseline of $|\Delta m_{\mathrm{red}} - \Delta m_{\mathrm{macro}}| \lesssim 0.3$. Further simulations are required to determine if these thresholds are universally applicable. However, even when these criteria are applied, the technique may still overestimate accretion disc sizes by roughly a factor of 1.5 to 2.0.

We have conducted only a preliminary exploration of these selection effects here. In particular, we note that the limits quoted in the previous paragraph were estimated using one specific set of microlensing parameters, appropriate for MG 0414+0534, and assuming that all of the microlensing was occurring in the saddle point image. These effects need to be systematically explored across astrophysically interesting parameter space if we are to confidently use the single-epoch technique for constraining quasar accretion discs. Detailed analysis of the impact of these effects on mock observations would allow us to construct more appropriate priors on our Bayesian measurements. We will pursue this task in a subsequent paper.

REFERENCES

Abajas C., Mediavilla E., Muñoz J. A., Popović L. Č., Oscoz A., 2002, ApJ, 576, 640

Abramowicz M. A., Czerny B., Lasota J. P., Szuszkiewicz E., 1988, ApJ, 332, 646

Agol E., Krolik J. H., 2000, ApJ, 528, 161

Anguita T., Schmidt R. W., Turner E. L., Wambsganss J., Webster R. L., Loomis K. A., Long D., McMillan R., 2008, A&A, 480, 327

Bade N., Siebert J., Lopez S., Voges W., Reimers D., 1997, A&A, 317, L13

Bate N. F., Fluke C. J., 2012, ApJ, 744, 90

Bate N. F., Webster R. L., Wyithe J. S. B., 2007, MNRAS, 381, 1591

Bate N. F., Floyd D. J. E., Webster R. L., Wyithe J. S. B., 2008, MNRAS, 391, 1955

Bate N. F., Floyd D. J. E., Webster R. L., Wyithe J. S. B., 2011, ApJ, 731, 71

Blackburne J. A., Pooley D., Rappaport S., Schechter P. L., 2011, ApJ, 729, 34

Blackburne J. A., Kochanek C. S., Chen B., Dai X., Chartas G., 2014, ApJ, 789, 125

Cackett E. M., Chiang C.-Y., McHardy I., Edelson R., Goad M. R., Horne K., Korista K. T., 2018, ApJ, 857, 53

Chantry V., Sluse D., Magain P., 2010, A&A, 522, A95

Chartas G. et al., 2016, Astron. Nachr., 337, 356

Dalal N., Kochanek C. S., 2002, ApJ, 572, 25

Eigenbrod A., Courbin F., Meylan G., Agol E., Anguita T., Schmidt R. W., Wambsganss J., 2008, A&A, 490, 933

Fausnaugh M. M. et al., 2016, ApJ, 821, 56

Floyd D. J. E., Bate N. F., Webster R. L., 2009, MNRAS, 398, 233

Frank J., King A., Raine D. J., 2002, Accretion Power in Astrophysics, 8th edn. Cambridge Univ. Press, Cambridge

Hewitt J. N., Turner E. L., Lawrence C. R., Schneider D. P., Brody J. P., 1992, AJ, 104, 968

Jackson N., Tagore A. S., Roberts C., Sluse D., Stacey H., Vives-Arias H., Wucknitz O., Volino F., 2015, MNRAS, 454, 287

Jiang Y.-F. et al., 2017, ApJ, 836, 186

Jiménez-Vicente J., Mediavilla E., Muñoz J. A., Kochanek C. S., 2012, ApJ, 751, 106

Jiménez-Vicente J., Mediavilla E., Kochanek C. S., Muñoz J. A., Motta V., Falco E., Mosquera A. M., 2014, ApJ, 783, 47 (JV14)

Jiménez-Vicente J., Mediavilla E., Kochanek C. S., Muñoz J. A., 2015a, ApJ, 799, 149

Jiménez-Vicente J., Mediavilla E., Kochanek C. S., Muñoz J. A., 2015b, ApJ, 806, 251

Katz C. A., Moore C. B., Hewitt J. N., 1997, ApJ, 475, 512

Keeton C. R., 2001, preprint (arXiv:astro-ph/0102340)

Kochanek C. S., Dalal N., 2004, ApJ, 610, 69

Krist J. E., Hook R. N., Stoehr F., 2011, in Kahan M. A., ed., Optical Modeling and Performance Predictions V. SPIE, Bellingham, p. 81270J

LSST Science Collaboration, 2009, preprint (arXiv:0912.0201)

MacLeod C. L. et al., 2012, ApJ, 753, 106

MacLeod C. L., Jones R., Agol E., Kochanek C. S., 2013, ApJ, 773, 35

MacLeod C. L. et al., 2015, ApJ, 806, 258

Mao S., Schneider P., 1998, MNRAS, 295, 587

Mediavilla E. et al., 2009, ApJ, 706, 1451

Minezaki T., Chiba M., Kashikawa N., Inoue K. T., Kataza H., 2009, ApJ, 697, 610

Morgan N. D., Caldwell J. A. R., Schechter P. L., Dressler A., Egami E., Rix H.-W., 2004, AJ, 127, 2617

Morgan C. W., Kochanek C. S., Morgan N. D., Falco E. E., 2010, ApJ, 712, 1129

Mortonson M. J., Schechter P. L., Wambsganss J., 2005, ApJ, 628, 594

Mosquera A. M., Kochanek C. S., 2011, ApJ, 738, 96

Mosquera A. M., Muñoz J. A., Mediavilla E., Kochanek C. S., 2011, ApJ, 728, 145

Motta V., Mediavilla E., Rojas K., Falco E. E., Jiménez-Vicente J., Muñoz J. A., 2017, ApJ, 835, 132

Muñoz J. A., Mediavilla E., Kochanek C. S., Falco E. E., Mosquera A. M., 2011, ApJ, 742, 67

O'Dowd M., Bate N. F., Webster R. L., Wayth R., Labrie K., 2011, MNRAS, 415, 1985

O'Dowd M. J., Bate N. F., Webster R. L., Labrie K., Rogers J., 2015, ApJ, 813, 62

O'Dowd M., Bate N. F., Webster R. L., Labrie K., King A. L., Yong S.-Y., 2018, MNRAS, 473, 4722

Ofek E. O., Rix H.-W., Maoz D., 2003, MNRAS, 343, 639

Oguri M., Marshall P. J., 2010, MNRAS, 405, 2579

Patnaik A. R., Browne I. W. A., Walsh D., Chaffee F. H., Foltz C. B., 1992, MNRAS, 259, 1P

Patnaik A. R., Kemball A. J., Porcas R. W., Garrett M. A., 1999, MNRAS, 307, L1

Peng C. Y., Ho L. C., Impey C. D., Rix H.-W., 2002, AJ, 124, 266

Pooley D., Blackburne J. A., Rappaport S., Schechter P. L., 2007, ApJ, 661, 19

Pooley D., Rappaport S., Blackburne J. A., Schechter P. L., Wambsganss J., 2012, ApJ, 744, 111

Rojas K., Motta V., Mediavilla E., Falco E., Jiménez-Vicente J., Muñoz J. A., 2014, ApJ, 797, 61

Schechter P. L., Wambsganss J., 2002, ApJ, 580, 685

Schechter P. L., Pooley D., Blackburne J. A., Wambsganss J., 2014, ApJ, 793, 96

Shakura N. I., Sunyaev R. A., 1973, A&A, 24, 337 (SS)

Sluse D., Chantry V., Magain P., Courbin F., Meylan G., 2012a, A&A, 538, A99

Sluse D., Hutsemékers D., Courbin F., Meylan G., Wambsganss J., 2012b, A&A, 544, A62

Starkey D. et al., 2017, ApJ, 835, 65

Thompson A. C., Fluke C. J., Barnes D. G., Barsdell B. R., 2010, New A, 15, 16

Vanden Berk D. E. et al., 2001, AJ, 122, 549

Vernardos G., Fluke C. J., Bate N. F., Croton D., 2014, ApJS, 211, 16

Vernardos G., Fluke C. J., Bate N. F., Croton D., Vohl D., 2015, ApJS, 217, 23

Wayth R. B., O'Dowd M., Webster R. L., 2005, MNRAS, 359, 561

This paper has been typeset from a TEX/LATEX file prepared by the author.